

# MaRS: Mars Express Radio Science Experiment

M. Pätzold<sup>1</sup>, S. Tellmann<sup>1</sup>, T. Andert<sup>1</sup>, L. Carone<sup>1</sup>, M. Fels<sup>1</sup>, R. Schaa<sup>1</sup>, C. Stanzel<sup>1</sup>, I. Audenrieth-Kersten<sup>1</sup>, A. Gahr<sup>1</sup>, A.-L. Müller<sup>1</sup>, B. Stracke<sup>1</sup>, D. Stupar<sup>1</sup>, C. Walter<sup>1</sup>, B. Häusler<sup>2</sup>, S. Remus<sup>2</sup>, J. Selle<sup>2</sup>, H. Griebel<sup>2</sup>, W. Eidel<sup>2</sup>, S. Asmar<sup>3</sup>, G. Goltz<sup>3</sup>, D. Kahan<sup>3</sup>, J.-P. Barriot<sup>4</sup>, V. Dehant<sup>5</sup>, M. Beuthe<sup>5</sup>, P. Rosenblatt<sup>5</sup>, Ö. Karatekin<sup>5</sup>, V. Lainey<sup>5</sup>, G.L. Tyler<sup>6</sup>, D. Hinson<sup>6</sup>, R. Simpson<sup>6</sup> & J. Twicken<sup>6</sup>

<sup>1</sup> *Institut für Geophysik und Meteorologie, Universität zu Köln, D-50923 Köln, Germany; now at Rheinisches Institut für Umweltforschung, Abt. Planetenforschung an der Universität zu Köln, D-50931, Germany*  
Email: [paetzold@geo.uni-koeln.de](mailto:paetzold@geo.uni-koeln.de)

<sup>2</sup> *Institut für Raumfahrttechnik, Universität der Bundeswehr München, D-85577 Neubiberg, Germany*

<sup>3</sup> *Jet Propulsion Laboratory, California Institute of Technology, 4800 Oak Grove Drive, Pasadena, CA 91009, USA*

<sup>4</sup> *Observatoire Midi Pyrenees, F-31401 Toulouse, France*

<sup>5</sup> *Observatoire Royal, B-1180 Brussels, Belgium*

<sup>6</sup> *Space, Telecommunication & Radioscience Laboratory, Department of Electrical Engineering, Stanford University, Stanford CA 95305, USA*

**The Mars Express Radio Science Experiment (MaRS) started regular operations in April 2004. The experiment employed radio occultation during two occultation seasons in April-August 2004 and December 2004 to sound the neutral martian atmosphere to derive vertical density, pressure and temperature profiles as functions of height, and to sound the ionosphere to derive vertical ionospheric electron density profiles. Both profile types were monitored as functions of time in order to determine diurnal variations and, in the case of the ionosphere, dependence on solar wind conditions. MaRS also determined the dielectric and scattering properties of the martian surface in specific target areas by using bistatic radar, determining gravity anomalies during pericentre passes at altitudes of 250 km for investigations of the structure and evolution of the crust and lithosphere, and sounding the solar corona during the superior conjunction of Mars with the Sun from mid-August to mid-October 2004. This chapter gives, as intended by the project, an overview of the observations from April 2004 to mid-2005, and presents examples and first results.**

Mars Express was injected into orbit around Mars on 25 December 2003; the science instrument commissioning phase began in January 2004, after arrival in the operational orbit, and lasted until June 2004. Since then, Mars Express has been conducting regular observations of the planet and environs. The primary mission, which ended in November 2005, was succeeded by an extended mission.

The Mars Express Orbiter Radio Science Experiment (MaRS) is employing radio occultation (i) to sound the neutral martian atmosphere to derive vertical density, pressure and temperature profiles as functions of height, and (ii) to sound the ionosphere to derive vertical ionospheric electron density profiles. Both types of profiles may be monitored as functions of time to determine diurnal and seasonal variations and, in the case of the ionosphere, dependence on solar wind conditions. MaRS is also (iii) determining the dielectric and scattering properties of the surface in specific target

## 1. Introduction

Table 1. Expected/actual observations from January 2004 to mid-2005.			
Observation Type	Observations (expected/accomplished)		
	Jan-Jun 2004	Jul-Dec 2004	Jan-Jun 2005
Radio Occultation Ingress	92/53	45/32	180/3
Radio Occultation Egress	92/0	45/0	180/0
Bistatic Radar	26/2	26/0	26/4
Gravity	20/0	30/12	60/8
Phobos	1/0	N/A	2/0
Solar Conjunction	N/A	60/39	N/A

areas by using bistatic radar, (iv) determining gravity anomalies for investigation of the structure and evolution of the crust and lithosphere, (v) determining the mass and (indirectly) density of the moon Phobos, and (vi) sounded the solar corona during the superior conjunction of Mars with the Sun.

Operational limitations imposed by reduced power output from the solar panels and by pointing conflicts with the imaging instruments around pericentre that were not anticipated or fully appreciated meant that the total number of MaRS observations was significantly reduced from original estimates (Table 1). Primary factors include limited transmitter operation while the satellite was in solar eclipse (which is highly correlated with Earth occultation), reduced pericentre gravity coverage and Phobos flybys to accommodate other instruments requiring nadir pointing, and scheduling changes associated with the delayed MARSIS antenna deployment. No egress occultations were observed, for example, because of concerns about changes in the transmitter state while the spacecraft was hidden from view. Since some observations such as bistatic radar required support from the heavily booked NASA Deep Space Network (DSN) 70 m antennas, late planning changes owing to technical issues or observation conflicts with other instruments often precluded rescheduling of those facilities, with the loss of the experiment opportunity.

MaRS defined its own observation phases when the focus was on occultation, gravity or the solar corona. The first occultation season to sound the atmosphere/ionosphere lasted from April to mid-August 2004 and merged at the end with the start of the solar conjunction phase (mid-August to mid-October 2004). From mid-October to early December 2004, the focus should have been on gravity observations around pericentre but competition with the imaging instruments was strong and only a fraction of the expected observations was accomplished. The second occultation season, starting in December 2004, had to be terminated prematurely in early January owing to power problems during eclipses. Similarly, the observation of gravity targets in the northern polar regions and the entire third occultation season until April 2005 was abbreviated or could not be performed, respectively.

This chapter provides an overview and examples of the observations made in 2004 and the first half of 2005. The analysis of the atmosphere/ionosphere, bistatic radar and gravity results, for example, is an ongoing and tedious process and is most effective when applied to the results from many observations together rather than from single orbits.

## 2. Planning Radio Science Observations

A Radio-Science Simulator (RSS) was developed at the Universität der Bundeswehr (University of the German Federal Armed Forces) in Munich, Germany, to simulate, plan and analyse RS experiments on interplanetary space missions. This fast software tool is based on the programming language Matlab/Simulink. It provides computations of expected Doppler shifts of the radio carriers and range information crucial for the analysis of RS experiments, based on the precise determinations of planetary and spacecrafts ephemerides data. Furthermore, reference systems and time bases, allowing for the effects of the special and general theories of relativity, need to be incorporated to ensure the high precision required. Similar simulations for missions like Venus Express and Rosetta are possible without changing the software architecture.

Since the orbit insertion of Mars Express, several hundred RS measurements, including occultation, bistatic radar, gravity and solar corona experiments, have been planned and analysed using the RSS software. The following fundamental calculations are performed by the RSS:

- state vectors of spacecraft;
- planetary ephemerides;
- visibilities from the various ground stations involved;
- time of Earth occultations and the entry and exit locations;
- attitude manoeuvres for bistatic radar and occultation experiments.

These calculations require the usage of a large number of reference systems. Examples are the Earth-fixed geocentric International Terrestrial Reference System (ITRS) and the inertial International Celestial Reference System (ICRS), with its fundamental plane closely aligned with the mean Earth equator at the J2000 standard epoch. The transformation between the two systems includes planetary and lunisolar precession, Earth's rotation, nutation, polar motion and plate tectonics. Further details are discussed in Häusler et al. (2003a).

Graphical user interfaces (GUIs) were designed to facilitate the selection and linkage of various modules. Depending on input parameters, the appropriate modules are enabled and configured. The orbit module is one of the main parts of the software tool; it determines the parameters of the spacecraft orbit, including the gravitational interactions among the Sun, planets and moons of the Solar System, pressure of the solar photons and planetary albedo, and the higher moments of the gravitational potential of the central body. Computed state vectors (position and velocity) of the spacecraft then serve as input for other modules. Alternatively, orbit files for mission planning and reconstructed orbit files provided by ESA can also be read in by the software and made available to other modules.

For various calculations within the RSS, a continuous determination of state vectors for bodies in the Solar System is required. The algorithms use the JPL DE 405 ephemeris model based on J2000 coordinates. The module also takes into account the effects of the light travel time to determine the light-time corrected vector between the ground station and the spacecraft.

The ground station module determines the exact time of the start and end of spacecraft visibility at the ground stations using the output data of the orbit and ephemeris module. Usually, an angle of  $10^\circ$  above the horizon is assumed for the beginning of the recording track. Locations of ESA's New Norcia (NNO, Australia) ground station and all DSN antennas are incorporated into the database. The occultation module determines the times of atmospheric ingress and egress of the spacecraft radio signals, assuming an elliptical shape of the planetary body.

The bistatic radar module computes the location of the specular point on the surface of an elliptical planetary body. Target regions on the surface of the planet with special scientific interest may be defined. The module is able to select all possible observation periods that meet the specular reflection criteria, while allowing for special ground station and operational constraints.

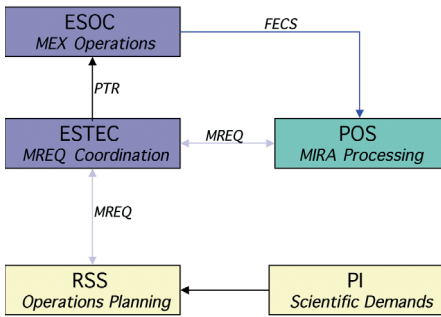


**Fig. 1. Planning tools and decision paths involved in the planning and operation of MaRS.** The Principal Investigator initiates an experiment simulation at the Radio Science Simulator (RSS). The MaRS team generates with the Parsifal software (developed by the Payload Operations Service, POS) radio science specific request files (MREQs) for ESTEC for further coordination. The Mars Express (MEX) Instrument Resource Analyser (MIRA) software using the Flight Dynamics Events and Communications Skeleton (FECS) from ESOC was developed by POS to identify spacecraft resource and instrument conflict situations. In the ideal case, conflict-free experiment operations can be carried out by ESOC.

### 3. Assessment of Carrier Frequency and Range Background Noise

The output of the occultation, bistatic radar, gravity and solar corona modules is used to generate request files for Mission Operations in a format defined by ESA. The request files are checked and adjusted in a complicated and time-consuming process to meet the specific Mars Express mission constraints defined by ESA. The result is the input for the mission planning process (Fig. 1).

Frequency shifts in the one-way and two-way modes depend on the relative velocity between transmitter and receiver (Doppler effect), typically of the order of 30 km/s, on perturbations by gravity potentials, other non-gravitational forces acting on the spacecraft, and the effects from special and general relativity. The RSS Doppler module takes into account terms up to order  $(\beta^2 = v/c)^2$  (Häusler et al., 2003a):

$$\frac{f_E}{f_S} \approx 1 - \hat{\mathbf{n}} \cdot (\hat{\mathbf{a}}_E - \hat{\mathbf{a}}_S) - \frac{1}{2}(\beta_S^2 - \beta_E^2) - (\hat{\mathbf{n}} \cdot \hat{\mathbf{a}}_S)(\hat{\mathbf{n}} \cdot \hat{\mathbf{a}}_E) + (\hat{\mathbf{n}} \cdot \hat{\mathbf{a}}_S)^2 + \frac{1}{c^2}(\phi_S - \phi_E) \quad (1)$$

assuming a system  $S$  (spacecraft) is transmitting the frequency  $f_S$ , and a system  $E$  (Earth ground station) receives the frequency  $f_E$ . Here, we define  $\hat{\mathbf{a}} = v/c$  with  $\hat{\mathbf{n}}$  being a unit vector pointing from  $(S)$  to  $(E)$ , i.e. in the direction of the signal propagation at the time the signal is radiated.  $v_S$  is the coordinate velocity of the spacecraft  $S$  and  $v_E$  is the coordinate velocity of the ground station on Earth at the time of signal emission and reception, respectively. The coordinate system used is the Solar System barycentric system. All relative velocities must be Lorentz-transformed.  $\phi_E$  and  $\phi_S$  are the gravitational potentials of  $E$  and  $S$ , respectively. The potential of the ground station contains the centrifugal potential of Earth. For one-way propagation, the contribution of the gravitational potentials (gravitational redshift) can be significant and can reach approximately 30 Hz at the X-band. The Doppler predictions are compared with the received Doppler data, forming the Doppler residuals, which represent the basis for later scientific analysis, leading to planetary atmospheric parameters such as temperature, density and pressure.

More than a year of MaRS operations provides the opportunity to analyse the performance of the experiment by comparing the actual measurements during different time periods and at different Earth–spacecraft distances with predictions based on link analyses.

As extensively discussed in Pätzold et al. (2004), the performance of a radio science experiment at the radio frequency level can be expressed by two quantities: the Doppler frequency and the ranging values recorded at the ground station. The quality of these recordings determines the accuracy of sounding planetary atmospheres and ionospheres, the accuracy of the determination of planetary gravity field coefficients, and the detail of which effects of the propagation of radio wave propagation in the solar corona/solar wind plasma can be studied. Several parameters have to be carefully considered when making such a comparison: the spacecraft–Earth distance, the configurations of the onboard transponder and the ground station.

Data were studied from three time periods (June 2005, January 2005, August 2004), when the MaRS experiment was configured in the coherent TWOD mode (X-uplink, X- and S-downlink) for global gravity measurements at the orbit’s apocentre. The data were recorded at ESA’s NNO. The corresponding spacecraft–Earth distances were 1.1, 2.1 and 2.5 AU. The radio frequency parameters of the ground station and the spacecraft transponder are given in the MEX Space/Ground Interface Control Document SGICD (2003). The transponder phase noise and group delay performances as measured on the ground are summarised in Remus et al. (2001) and Häusler et al. (2003b).

Since the measurement made on 7 August 2004 near 2.5 AU took place only about a month before superior solar conjunction (17 September 2004), the contribution of the solar corona plasma to the Doppler measurement was substantial. A coarse

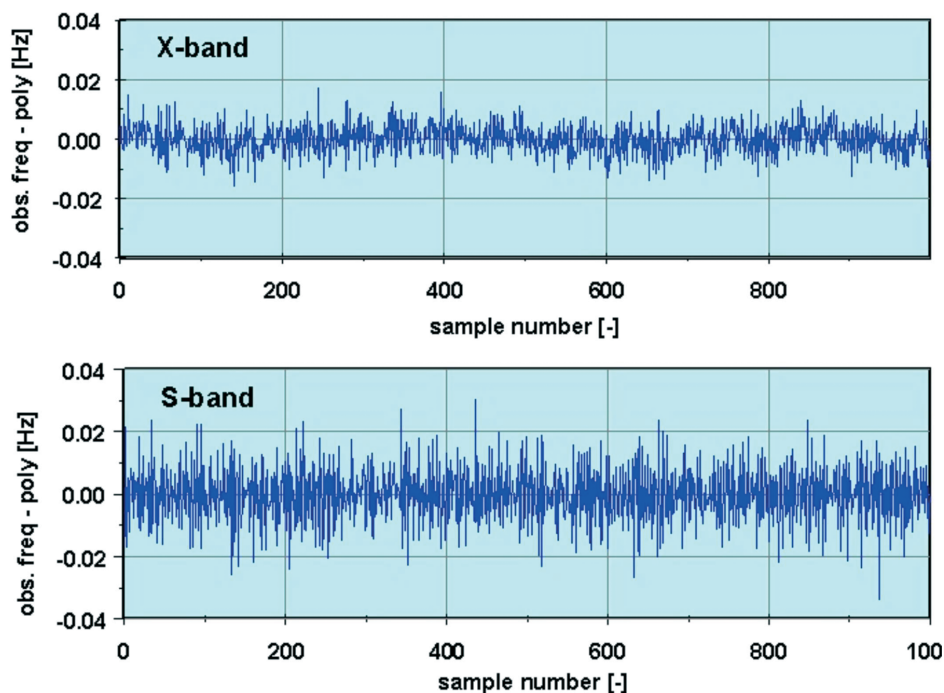


Fig. 2 X-band (upper panel) and S-band (lower panel) frequency residuals recorded in orbit 1775/1776 at orbit apocentre. The  $1\sigma$  standard deviation at 1 s integration time is 5.6 mHz at X-band and 9.4 mHz at S-band, which correspond to  $201.8 \mu\text{m/s}$  and  $1227.5 \mu\text{m s}^{-1}$  Doppler velocity noise, respectively. See Table 1 for frequency stability.

Doppler noise	$\sigma_v$ [ $\mu\text{m/s}$ ] X-Band $\Delta t = 1 \text{ s}$	$\sigma_v$ [ $\mu\text{m/s}$ ] S-Band $\Delta t = 1 \text{ s}$	ALLAN DEV [ $10^{-13}$ ] @ 1 s		ALLAN DEV [ $10^{-13}$ ] @ 10 s		ALLAN DEV [ $10^{-13}$ ] @ 100 s	
			X	S	X	S	X	S
Orbit: 1775/1776 DOY 154 1.1 AU	201.8	1227.5	6.7	13.5	2.4	1.7	1.1	0.4
Orbit: 1282/1283 DOY 016 2.1 AU	331.4	3043.4	11.4	30.1	3.6	7.6	2.5	4.2
Orbit: 701/702 DOY 220 2.5 AU	514.3	3808.7	17.8	38.3	5.4	10.3	2.7	5.3

estimate of the average solar contribution to the standard deviation of the Doppler measurement error, which is based on the work of Woo & Armstrong (1979), is given in DSMS (2000) and was included in this analysis. The predicted Doppler and range values were subtracted from the Doppler and group delay (ranging) measurements recorded at the ground station. These residuals were detrended and used in this analysis.

### 3.1 Doppler Measurements

As an example, Fig. 2 shows Doppler residuals taken from orbit 1775/1776 on day-of-year (DOY) 154 (3 June 2005) sampled at 1 s integration time over a time period of 1000 s.

The three sets of Doppler data for the above three passes were sampled at 1 s integration time for a time period of 5000 s per pass. Table 2 shows the correspondingly converted values of the standard deviation  $\sigma_v$  ( $\mu\text{m s}^{-1}$ ) of the velocity error. The Allan deviation values at 1, 10 and 100 s integration times are shown for completeness.

Table 3. Doppler noise ( $\mu\text{m/s}$ ) predicted on the basis of radio link analyses and expected average contributions of solar corona plasma effects in comparison with measured values.

Doppler Noise	$\sigma_v$ [ $\mu\text{m/s}$ ] X/X-Band $\Delta t = 1$ s Prediction	$\sigma_v$ [ $\mu\text{m/s}$ ] X/X-Band $\Delta t = 1$ s Expected Average Solar Plasma Contribution	$\sigma_v$ [ $\mu\text{m/s}$ ] X/S-Band $\Delta t = 1$ s Prediction	$\sigma_v$ [ $\mu\text{m/s}$ ] X/S-Band $\Delta t = 1$ s Expected Average Solar Plasma Contribution
Orbit: 1775/1776 DOY 154 1.1 AU	145	$\geq 0$	1930	0
	Predicted RSS Noise: 145		Predicted RSS Noise: 1930	
	Measured Noise: 201.8		Measured Noise: 1227.5	
Orbit: 1282/1283 DOY 016 2.1 AU	276	0	3680	0
	Predicted RSS Noise: 276		Predicted RSS Noise: 3680	
	Measured Noise: 331.4		Measured Noise: 3043.4	
Orbit: 701/702 DOY 220 2.5 AU	329	390	4380	3320 <sup>(a)</sup>
	Predicted RSS Noise: 510		Predicted RSS Noise: 5496 <sup>(a)</sup>	
	Measured Noise: 514.3		Measured Noise: 3808.7	

<sup>(a)</sup> The X/S link values for the solar plasma noise contributions  $\sigma_v$  were derived by multiplying  $\sigma_v$  of the X/X link by a factor 8.

The measured Doppler noise can now be compared with the predicted Doppler noise based on a radio link analysis which takes into account additional average error contributions due to solar corona plasma effects (DMS, 2000); see Table 3. Coronal plasma propagation values are applicable for Sun–Earth–MEX angles of 5-27° and are applied therefore for orbit 701/702 only. The other orbits have Sun–Earth–MEX angles much larger than 27° and the solar plasma propagation contribution at X-band is neglected against the thermal effects in the onboard transponder and the ground station.

The radio link analysis assumed an operational configuration of the ground station and spacecraft transponder as given in SGCID and derives the predicted carrier-to-noise power ratio  $C/N$  of the ground station. This ratio allows us to determine the resulting Doppler velocity noise according to (Yuen, 1983):

$$\sigma_v = \frac{c}{4\pi f \Delta t} \sqrt{\frac{2BN_0}{C}} \tag{2}$$

$\Delta t$  is the Doppler integration time,  $2B$  the double-sided loop bandwidth of the receiver at the ground station (assumed to be 100 Hz),  $N_0$  the noise power density of the ground station,  $C$  the received RF-carrier power and  $c$  the velocity of light. No telemetry modulation was assumed for the S-band downlink. Table 2 shows both the predicted Doppler noise (including solar plasma contributions) and the measured Doppler noise. The transponder phase noise for the X/X configuration measured on ground during system testing was 100  $\mu\text{m/s}$  (Häusler et al., 2003b). This contribution is included in the radio link analysis and does not need to be considered separately.

The comparison of measurements with predicted (estimated) values shows excellent agreement (within a factor 1.4) considering the uncertainties involved in such a complex

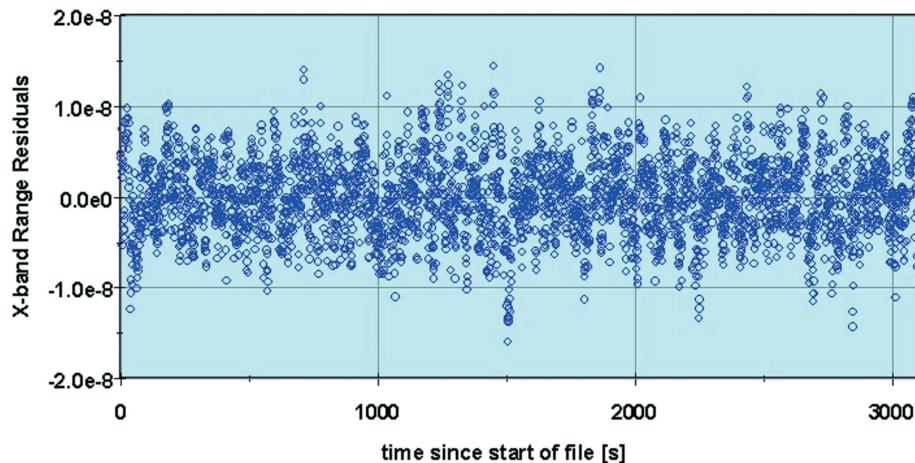


Fig. 3. The X-band ranging residuals recorded on orbit 1775/1776 at orbit apocentre. The  $1\sigma$  standard deviation is 4.3 ns, which corresponds to 1.3 m topocentric distance (distance ground station–spacecraft).

experiment as MaRS. There is also reasonable agreement with the predictions made earlier (Pätzold et al., 2004), which did not consider solar plasma effects.

One can conclude that the solar plasma noise begins to dominate the thermal noise contributions at Sun–Earth–MEX angles smaller than approximately  $30\text{--}50^\circ$ . For future operations it seems therefore worth considering for regions  $>30^\circ$  means for reducing the thermal noise contributions. This can be achieved by, for example, employing a smaller carrier loop bandwidth (30 Hz or 10 Hz) at the ground station.

### 3.2 Ranging observations

Ranging data taken in orbit 1775/1776 on DOY 154 (3 June 2005) are shown in Fig. 3. The data represent detrended values for X-band with a 1 s sampling rate for a time period of 3500 s.

The standard deviation  $\sigma_r$  ( $10^{-9}$  s) of the ranging measured during the above three passes and sampled at 1/s for 3500 s per pass is presented in Table 4. The ranging errors predicted by the radio frequency link analysis were derived according to Eq. (2) (Yuen, 1983) and are shown for comparison in Table 4.

$$\sigma_r \sim \frac{1}{8\sqrt{\Delta t \cdot f_T}} \cdot \frac{1}{\sqrt{P_R/N_0}} (s) \quad (3)$$

$\Delta t$  is the integration (correlation) time, determined by the ranging loop filter bandwidth set on the ground, which results effectively in a time constant of  $\sim 10$  s,  $f_T$  is the tone frequency (1 MHz),  $P_R$  and  $N_0$  are the available ranging signal power and power spectral density at the ground station, respectively.

Again, there is excellent agreement between predicted and measured values. However, no reliable models describing the solar plasma ranging noise contributions are available in the literature that could be incorporated in the analysis. It is estimated that, for X-band, average contributions at Sun–Earth–MEX angles  $>10^\circ$  do not exceed 1 ns, which would not alter the conclusions drawn so far.

The atmosphere and ionosphere can be sounded only when the spacecraft is going into occultation as seen from Earth. Prior to occultation, the radio signals (uplink to the spacecraft and downlink from the spacecraft) are propagating through the atmosphere. The observations start typically 20 min before the predicted occultation time and stop 3–5 min into occultation. The frequency and automatic gain control of the received radio signals at X-band and S-band are recorded at the ground station complexes

Ranging noise	Measured $\sigma_r$ [ $10^{-9}$ s] X-band	Predicted $\sigma_r$ [ $10^{-9}$ s] X-band
Orbit 1775/1776 DOY 154 1.1 AU	5.3	1.6
Orbit 1282/1283 DOY 016 2.1 AU	4.3	5.4
Orbit 701/702 DOY 220 2.5 AU	6.7	7.6

## 4. Observations of the Martian Atmosphere and Ionosphere

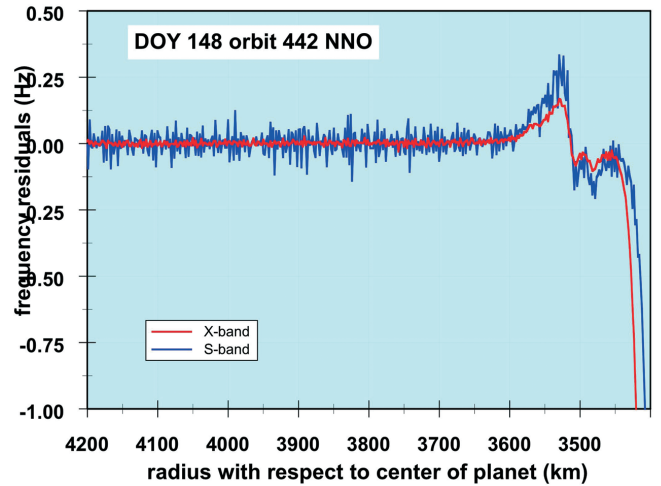
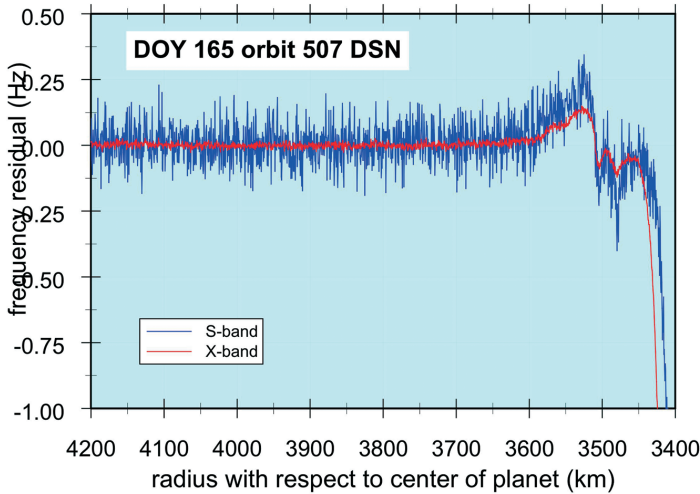


Fig. 4 (left). Frequency residuals at X-band (red) and S-band (blue) starting at a radius with respect to the centre of Mars of 4200 km before occultation (at radius 3380 km in this case). The frequency residuals are computed from the received frequency minus the predicted frequency based on the latest reconstructed orbit solution assuming no atmosphere/ionosphere. All deviations from zero are considered to be caused by the propagation of the radio waves through the ionosphere first (starting

visibly at radius 3750 km) and finally the atmosphere (starting at radius 3450 km). The final frequency shift at occultation is  $-10$  Hz. This occultation was recorded at DSN station 65 in Madrid on DOY 165, 2004 (orbit 507).

Fig. 5 (right). Same as Fig. 4 for a recording at the ESA ground station NNO on DOY 148, 2004 (orbit 442).

of the DSN or at NNO. Frequency residuals in both bands are computed from the observed received frequency and the predicted received frequency based on the latest reconstructed orbit solution.

Figures 4 and 5 show the frequency residuals for two occultations recorded at DSS 65 of the DSN (Fig. 4) and NNO (Fig. 5). The S-band has a higher noise by a factor of five, but both frequencies clearly show the result of ray bending due to propagation in the ionosphere first and then a large frequency decrease at the end of the observation due to propagation in the neutral atmosphere shortly before occultation. The frequency shift is finally up to  $-10$  Hz at the time of occultation.

Radio occultation studies of atmospheres can be understood in terms of ‘geometric’ or ‘ray’ optics refraction of signals travelling between spacecraft and ground stations. In a spatially varying medium, wherein the wavelength is very short compared to the scale of variation in refractive index, the direction of propagation of an electromagnetic wave always curves in the direction of increasing refractivity. Consequently, in a spherically symmetric atmosphere with gas refractivity proportional to the number density constantly decreasing with height, the radio path remains in a plane and bends about the centre of the system. The degree of bending depends on the strength of the refractivity gradient. This simple model approximates to a real atmosphere and is useful for understanding the basic phenomena of radio occultation (Fjeldbo, 1964).

The geometry is illustrated in Fig. 6, where the atmosphere is represented by the refractivity as a function of radius from the centre,  $\mu(r_0) = (v(r_0) - 1) \times 10^6$ , where  $v(r_0)$  is the refractive index and the bending can be described in terms of a total bending angle,  $\alpha$ , and a ray asymptote,  $a$ . The variation of the bending angle, ray asymptote and refractivity are linked through an Abel transform (Fjeldbo & Eshleman, 1968):

$$\alpha(a) = -2a \int_{r=r_0}^{\infty} \frac{1}{v} \frac{\partial v}{\partial r} \frac{\partial r}{\sqrt{(vr)^2 - a^2}} \tag{4}$$

where  $r_0 = \frac{a}{v(r_0)}$  is the ray periapse, and

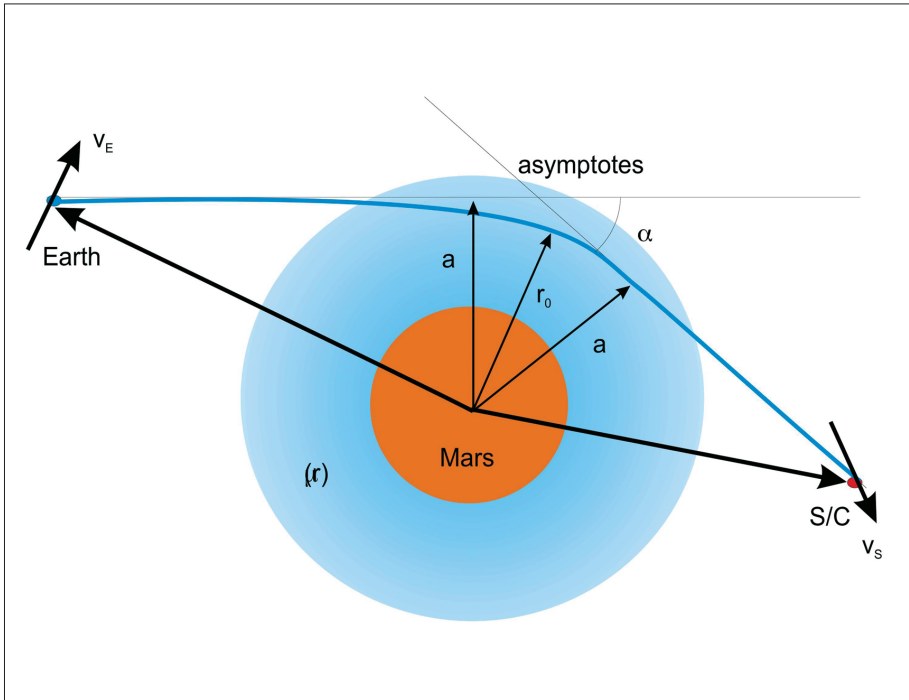


**Fig. 6. Planetary occultation geometry assuming a radially symmetric atmosphere. The bending of the microwave ray is caused by the gradient of the atmospheric refractivity  $\mu(r)$ .**

$$v(r_{01}) = \exp \left\{ -\frac{1}{\pi} \int_{a=a_1}^{a=\infty} \ln \left[ \frac{a}{a_1} + \sqrt{\left[ \left( \frac{a}{a_1} \right)^2 - 1} \right]} \right] \frac{d\alpha}{da} da \right\} - \quad \text{with } r_{01} = \frac{a}{v(r_{01})} \quad (5)$$

In this last expression,  $a_1$  represents the asymptotic miss distance for a ray whose radius of closest approach is  $r_{01}$ . Thus, for spherical atmospheres, if  $\alpha(a)$  is known, then the corresponding refractivity profile can be found exactly. For non-spherical geometry, alternative numerical solutions are available. The bending angle and the ray asymptote can be determined accurately by radio occultation to create an experimentally derived table of  $\alpha$  versus  $a$ , or  $\alpha(a)$ . For the two-way case, as for MEX, the method as described in Lipa & Tyler (1979) was used.

The atmospheric/ionospheric refractivity as a function of height  $\mu(h)$  (Fig. 7) depends on the local state of the atmosphere (density, temperature, pressure, electron density):

$$\mu(h) = C_1 \frac{p(h)}{T(h)} + C_3 \frac{N_e(h)}{f^2} \quad (6)$$

where  $p(h)$  and  $T(h)$  are the pressure and temperature as a function of height  $h$ , respectively.  $C_1 = 1.3077 \times 10^{-6}$  (Hinson et al., 1999) depends on the actual composition of the neutral atmosphere, and

$$C_3 = 10^{-6} \frac{e^2}{\epsilon_0 m_e} = 40.31 \cdot 10^{-6} \frac{s^2}{m^3} \cdot N_e(h)$$

$N_e(h)$  is the electron density of the ionosphere and  $f$  is the sounding frequency of the radio carrier wave.

In the neutral atmosphere, refractivity is linearly related to the mass density of the atmospheric constituents (Fjeldbo & Eshleman, 1968) and follows

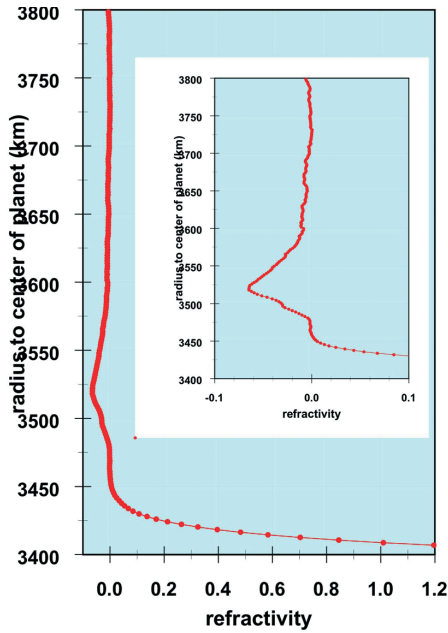


Fig. 7. Refractivity profile recorded on 12 June 2004 at NNO. The profile covers an altitude range of 400 km. Positive refractivity is from the neutral atmosphere, negative refractivity from the ionosphere. There is a short range between 50 km and 70 km altitude of zero refractivity where the neutral atmosphere is too thin and the ionisation is too low to be sensitive for microwaves. The ionosphere region is enlarged in the inset. The refractivity in the ionosphere is directly proportional to electron density ( $L_s = 46.1^\circ$ , solar zenith angle =  $18.5^\circ$ , local time = 17:09; coordinates  $271^\circ\text{E}$ ,  $24^\circ\text{N}$ ).

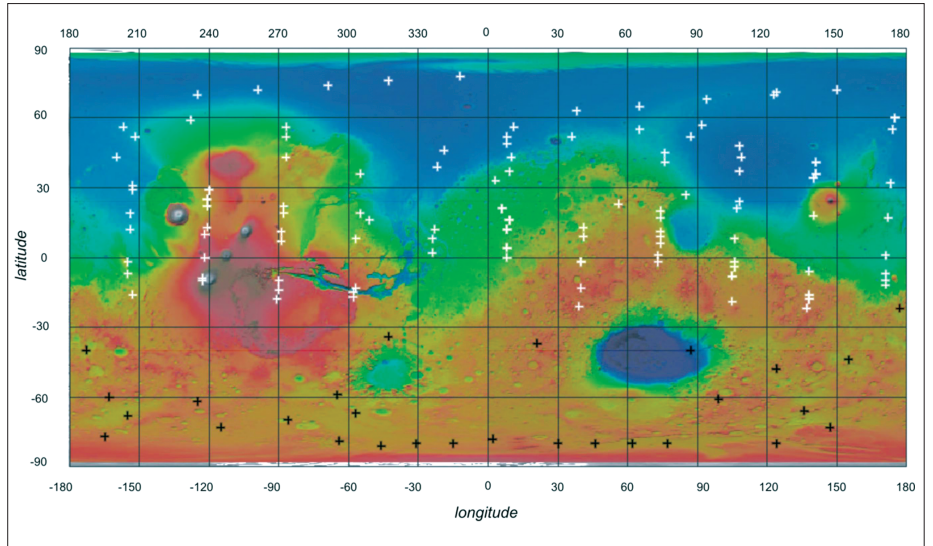


Fig. 8. Footprints of the occultation profiles from the first occultation season (white crosses) and the second occultation season (black crosses).

$$\mu(h) = \kappa N(h) = C_i k_B N(h) \quad (7)$$

where  $\kappa$  is the refractive volume,  $N(h)$  is the molecular number density and  $k_B$  is the Boltzmann constant. The refractivity of free electrons is given by the third term in Eq. (6), which allows easy conversion of refractivity into electron number densities.

In order to interpret the refractivity in terms of gas parameters, the pressure and temperature are calculated assuming hydrostatic equilibrium, for example, from

$$p(h) = \langle m \rangle \int_h^\infty g(h) N(h) dh \quad (8)$$

and

$$T(h) = \frac{p(h)}{k_B N(h)} \quad (9)$$

where  $g(h)$  is the acceleration of gravity and  $\langle m \rangle$  is the mean molecular mass. Formal use of these equations requires *a priori* knowledge of the atmospheric composition.

The separation of the effects of the ionosphere and the neutral atmosphere on the radio link is feasible by (a) using a dual-frequency downlink, (b) the opposite sign of the refractive index if the radio signal propagates in ionised or neutral media, and (c) the fact that the peak heights of the ionosphere and the detectable neutral atmosphere are well separated. Negative refractivity results from the ionised plasma in the ionosphere and is proportional to the electron number density; positive refractivity is a property of the neutral atmosphere (Fig. 7).

It is feasible to retrieve two refractivity profiles with Mars Express for each radio carrier frequency at S-band and X-band. S-band is expected to be more sensitive to the negative refractivity (ionosphere) by a factor (11/3) compared with X-band, while the positive refractivity (neutral atmosphere) is essentially independent of the frequency.

The spacecraft–Earth radio ray path will cross through the sensible ionosphere quickly (in about a minute) before entering occultation (Figs. 4 and 5). The variation in Earth's ionosphere and the interplanetary medium is assumed to be slow for time scales shorter than a minute, so the observed changes in radio carrier properties are assumed to be due to and dominated by the martian ionosphere.

During the first occultation season, from April to mid-August 2004, MaRS retrieved about 100 profiles of pressure, temperature, neutral number density from the neutral atmosphere and electron density from the ionosphere. Another 32 profiles were obtained during the second occultation season (Fig. 8).

The dataset from the first occultation season may be divided into two parts: 13 profiles obtained in April 2004 (solar longitudes  $L_s = 13\text{--}21^\circ$ ) covering solar zenith angles from  $108^\circ$  to  $85^\circ$  at local morning times of about 04:30 to 05:15, and a second part of about 86 profiles ( $L_s = 32\text{--}74^\circ$ ) covering solar zenith angles from  $70^\circ$  to  $84^\circ$  at local late afternoon times at about 17:00.

Thirty-two profiles of the second occultation season were observed from 8 December 2004 to 4 January 2005. The observations in this season had to be terminated prematurely owing to the eclipse situation; two-thirds of the maximal possible occultations could not be observed.

#### 4.1 Profiles from the Neutral Atmosphere

Vertical profiles of pressure, temperature and number-density of the neutral atmosphere from near to the surface to about 50 km altitude were obtained at 05:00 local time at high latitudes in the Northern Plains ( $L_s = 13\text{--}21^\circ$ , early spring in the northern hemisphere) during sunrise and at local times of 17:00 from mid-latitudes in the northern hemisphere to the equator ( $L_s = 32\text{--}74^\circ$ ). MEX occultations therefore reach other latitudes and areas than Mars Global Surveyor (MGS) and provide valuable input for general circulation models (GCMs) of the atmosphere.

An example is shown in Fig. 9 from a low-latitude region at  $74^\circ\text{E}$ ,  $6.6^\circ\text{N}$  in mid-spring at 17:30 local time. The profiles range from the surface at 3397 km radius to about 40 km altitude. There is a gradual decrease in temperature from 230K at the surface to 140K at 40 km altitude. The error bars mark the confidence limits from the derivation process. The relative error in general for all profiles is 0.1% at the surface (fractions of a kelvin) to 10% at the top of the profile (15K). The blue open circles in Fig. 9 are temperatures and number-densities from the GCM derived at Laboratoire Météorologique Dynamique (LMD) in Paris (Angelats i Coll et al., 2005). The LMD GCM follows the observations well for profiles from the equator to the mid-latitudes in both hemispheres.

Strong deviations from the GCM can be identified in all observed profiles at polar latitudes during both local spring over the northern hemisphere (Fig. 10) and local winter (polar night) over the southern hemisphere (Fig. 11). These first-ever observations of the high latitudes at different local times to MGS observations provide valuable information for improving the GCMs of the martian atmosphere. Two examples from the early morning during local spring and from the polar night during local deep winter, at high northern and southern latitudes, respectively, are discussed below.

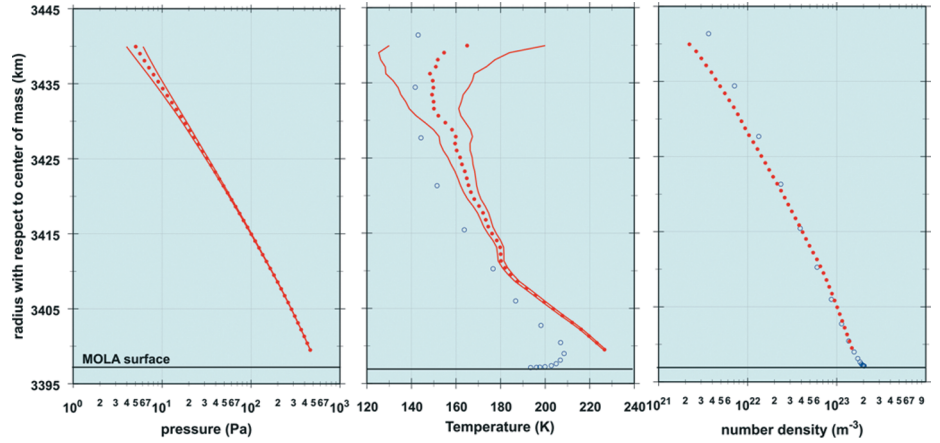
The temperature profile in Fig. 10 from  $290^\circ\text{E}$ ,  $74.5^\circ\text{N}$  in the Northern Plains at  $L_s = 21^\circ$  and 05:17 local time shows a very cold near-surface temperature of 156K at 2 km altitude; the atmosphere warms up to 168K at 6 km. An inversion layer at that altitude is present. The GCM follows essentially the same trend but at temperatures of about 10K higher. At 35 km altitude, a strong depletion of  $\text{CO}_2$  is experienced, as seen from the comparison of the GCM with the observed neutral number density.

Figure 11 shows profiles from high southern latitudes ( $47^\circ\text{E}$ ,  $-81^\circ\text{S}$ ) at local winter ( $L_s = 136^\circ$ ) at 14:30 local time. This is the polar night; the Sun is below the horizon for the entire sol and the atmosphere cools extremely during the polar night. The temperature is almost constant at 142K from the surface up to 35 km altitude. However, it is warmer than the atmosphere in the early morning at local spring (Fig. 10) at altitudes above 15 km. The GCM does not reflect the situation at all.

#### 4.2 Profiles from the Ionosphere

The electron density profile of the ionosphere is easily converted from the refractivity (the third term in Eq. 6). One observes a stable two-layer ionospheric structure (Fig. 12) at peak altitudes of approximately 110 km and 130 km for the M1 and M2 layers (the designation of layers follows Rishbeth & Mendillo, 2003), respectively,

**Fig. 9.** Derived pressure, temperature and number-density profiles from the surface (black line) to approximately 40 km altitude observed in orbit 570 on DOY 183, 2004, at (74°E, 6.6°N),  $L_s = 54.5^\circ$ , local time 17:30. The blue circles are temperature and density values extracted from the Mars atmosphere general circulation model from the Laboratoire Météorologie Dynamique (LMD), Paris.



**Fig. 10.** As Fig. 9, observed on orbit 314, DOY 109, 2004, at 290°E, 74.5°N,  $L_s = 21.1^\circ$ , local time 05 :17. This is the very early morning in early spring in the northern polar circle. The Sun is 5° above the horizon.

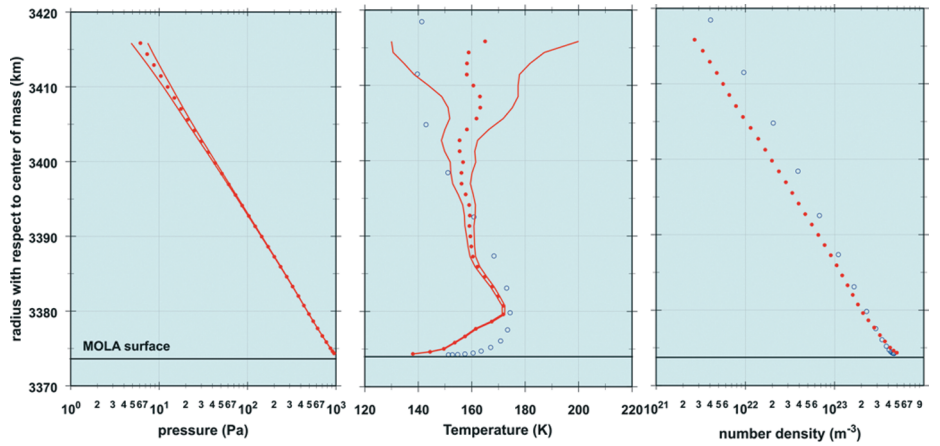
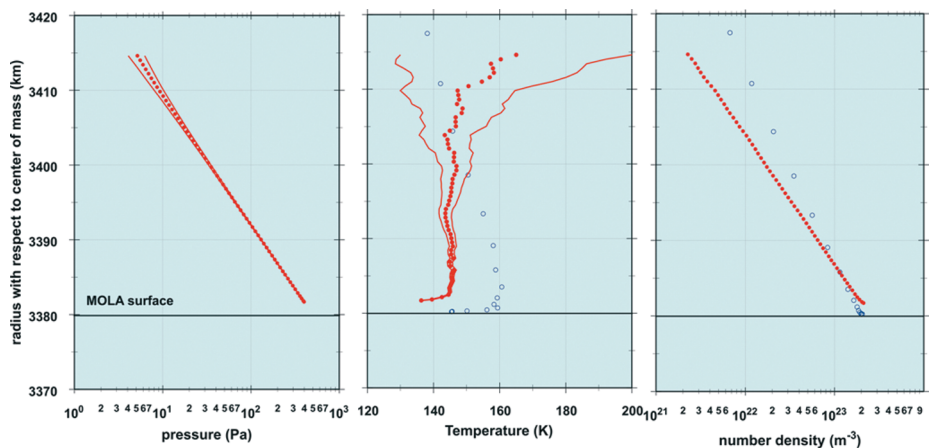


**Fig. 11.** As Fig. 9, observed on orbit 1219, on DOY 364, 2004, at 47°E, -81°N,  $L_s = 136.2^\circ$ , local time 14:30. This is an observation in high southern polar latitudes during the polar night (deep local winter). The Sun is below the horizon for the entire sol.



during the daytime. The peak electron densities are of the order of  $10^{11} \text{ el m}^{-3}$  for the M2 main layer (depending on the solar zenith angle) and approximately 50% less for the M1 layer. An ionopause can be identified at altitudes of 350 km (see Fig. 12), characterised by a strong gradient in electron density. The altitude of the ionopause is not the same for all profiles but changes in a range between 280 km and 650 km. In a few profiles, no ionopause can be identified at all.

Photochemical processes control the behaviour of the martian ionosphere around and below the main peak. *In situ* measurements made by the Viking landers showed

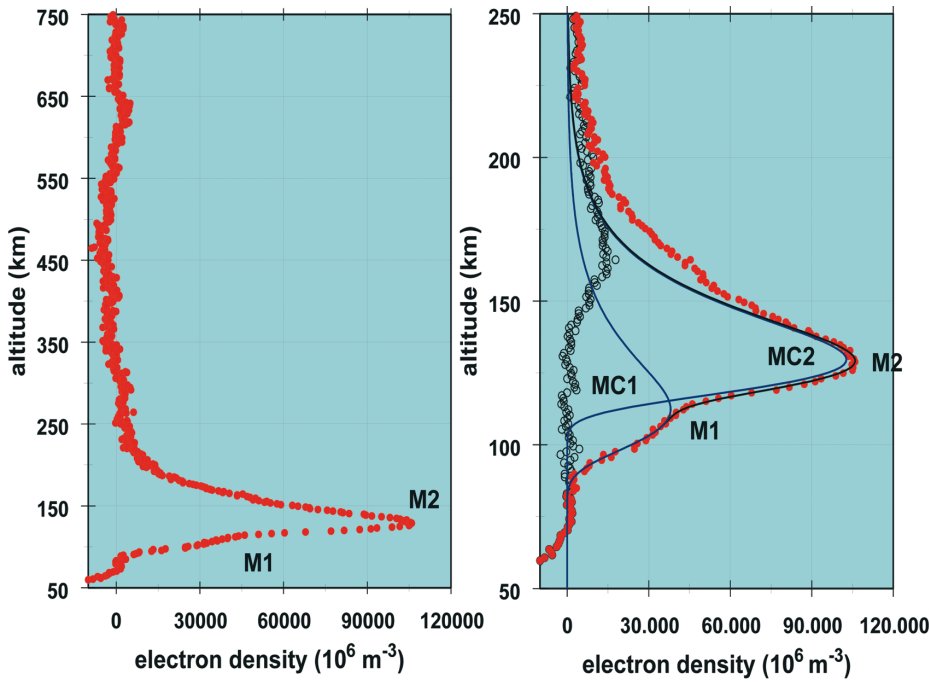


Fig. 12. Typical afternoon ionospheric profile recorded on DOY 171, 2004; solar zenith angle 80°, local time 17:00. Clearly identified (left panel) are the main peak M2 at 130 km altitude, the secondary peak M1 at 110 km, and an ionopause as the upper boundary of the ionosphere at 350 km altitude (in this case). The right panel shows the ionospheric layers in more detail. Two Chapman functions MC1 and MC2 are fitted to the individual layers M1 and M2, respectively (solid blue lines). The black solid line is the combination of MC1 and MC2 and fit the data of the lower ionosphere nicely. The fit is subtracted from the data in order to assess the electron density fluctuations of the lower ionosphere (open circles).

that the principal ion species in the ionosphere is  $O_2^+$  (Hanson et al., 1977), although the main neutral constituent is  $CO_2$ .  $CO_2^+$  is the ion generated by photoionisation in the extreme-UV but molecular processes form  $O_2^+$  rapidly and dominantly. The  $CO_2^+$  ion species contributes to the total ion density by 1% at the altitude of the main peak (135 km) and by 10% below the main peak. Transport processes become important in the topside ionosphere above the main peak for altitudes higher than 170 km.

The ionospheric profiles observed by Mars Express extend from 60 km altitude to about 1500 km. The MGS profiles range up to a maximal altitude of 400 km owing to the circular orbit radius; the MEX orbit is extremely elliptical and higher altitudes may be assessed. This allows the first in-depth study of the boundary between the topside of the ionosphere and the lower base of the solar wind interaction region within a complete electron density profile by the radio occultation method.

At Venus, this interaction region between the solar wind and the topside ionosphere is characterised by a strong gradient of electron density; it is called the ‘ionopause’. If we apply the same definition to Mars, two different ionopause features can be identified: (a) a strong electron density gradient of about  $1000 \text{ el m}^{-3} \text{ km}^{-1}$  over an altitude range of 20 km and (b) an electron density gradient of  $100\text{--}200 \text{ el m}^{-3} \text{ km}^{-1}$  over an altitude range of 80 km.

Two Chapman functions MC1 and MC2 were fitted to the electron profiles (Fig. 12, right panel):

$$N_e(z, \chi) = N_e(z, 0) \exp \left\{ \varepsilon_c \left( 1 - \frac{z - z_{\max}}{H} - \frac{e^{-\left(\frac{z - z_{\max}}{H}\right)}}{\cos \chi} \right) \right\} \quad (10)$$

where  $\varepsilon_c = 0.5$  for an ideal Chapman description,  $z_{\max}$  = altitude of the peak density,  $H = kT/mg$  the scale height of the neutral gas at temperature  $T$  and molecular mass  $m$ ,  $\chi$  = solar zenith angle and  $N_e(z, 0)$  = electron density at solar zenith angle  $\chi = 0^\circ$ .

The combination of the two Chapman functions MC1 plus MC2 fits the afternoon lower ionosphere and parts of the topside very nicely (Fig. 12). This is achieved for all afternoon profiles observed by MaRS. Electron density fluctuations are yielded

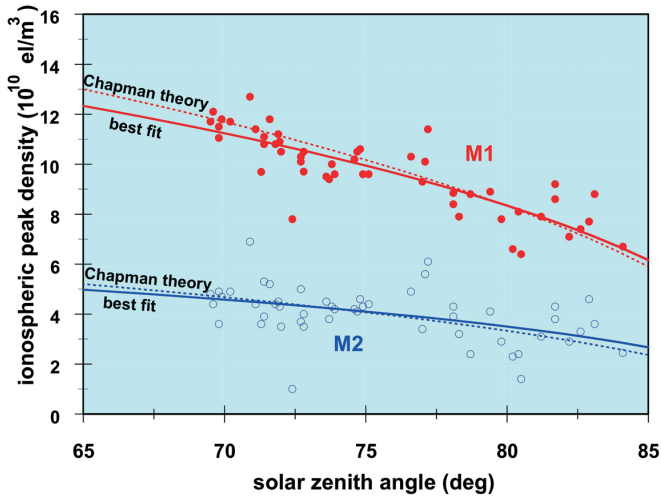


Fig. 13. Ionospheric peak density versus solar zenith angle from the profiles of the first occultation season. The dashed lines are the fits according to the Chapman theory (with fixed  $\epsilon = 0.5$ ). The solid lines are the best fits through all data.

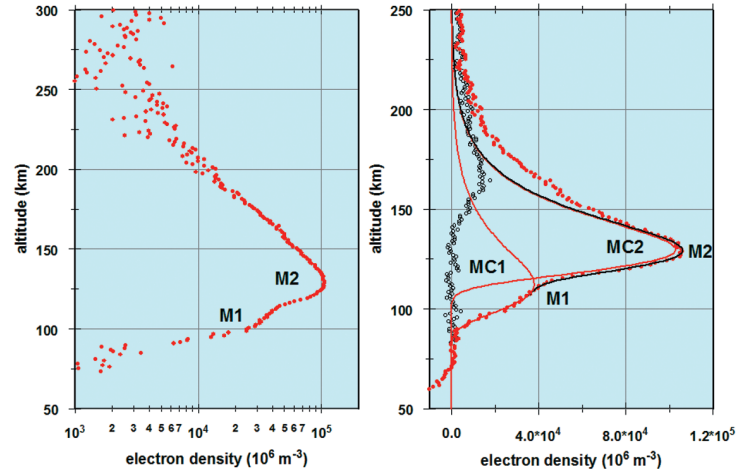


Fig. 14. Observation of the meteor layer below the lower layer on DOY 109, 2004, orbit 314. The black solid line is a combined Chapman fit to the data of the lower ionosphere. The open circles are the electron density residuals after subtracting the fit from the data. This fluctuation is smaller than the amplitude of the meteor layer.

by subtracting the Chapman fit from the observed electron density in the lower ionosphere. These fluctuations are of the same order of magnitude as the density fluctuation values at 600–700 km altitude, well outside the ionosphere and atmosphere. Although wave-like structures have been reported in the topside ionosphere (Wang & Nielson, 2003), it is concluded that these fluctuations are connected to inherent noise of the radio subsystem and/or radio signal propagation in the turbulent solar wind between spacecraft and Earth.

According to the Chapman theory, the peak electron density and altitude vary with solar zenith angle:

$$\begin{aligned} N_e(z_{\max}, \chi) &= N_e(z_{\max}, 0) \cos^{\epsilon_c} \chi \\ z_{\max}(\chi) &= z_{\max}(0) + H_n \ln(\cos \chi) \end{aligned} \quad (11)$$

Figure 13 shows the dependence of the M1 and M2 peak densities as a function of solar zenith angle for all afternoon profiles of occultation season 1. From Viking observations, Zhang et al. (1990) found  $\epsilon_c = 0.4$ , while Bauer & Hantsch (1989) found  $0.3 < \epsilon_c < 0.6$ . The best fits through the M1 and M2 peak density data points are achieved for  $\epsilon_c = 0.44$  and  $\epsilon_c = 0.4$ , respectively. In fact, the fits are indistinguishable for solar zenith angles greater than  $75^\circ$ . A clear deviation from Chapman theory can be identified only for solar zenith angles smaller than  $75^\circ$ .

Significant ionisation was observed well below the secondary peak M1 in about 10 out of 120 electron density profiles (Pätzold et al., 2005). This layer (Fig. 14) was predicted to be formed by ablation of metallic atoms from meteors entering the atmosphere (Molina-Cuberos et al., 2003). These metallic atoms are ionised by charge exchange. This layer, now called the ‘meteor layer’, appears to be local and sporadic for the MaRS observations. The amplitude of the meteor layer is many times larger than the standard deviation of the electron density fluctuations. The altitude of the meteor layer seems to be correlated with the altitude of the peak M1, suggesting that the ionosphere and the formation of the layer are related. The altitude of the peak ionisation of M1 moves to lower altitudes with decreasing solar zenith angle, the meteor layer follows the same trend. The martian atmosphere is of

sufficient density between 70 km and 100 km altitude to provide drag needed to heat and ablate meteorites. The density in Earth's atmosphere above 95 km, where the meteoritic layer has been found to be permanent (Kopp, 1997), is slightly higher than the neutral density of the martian atmosphere at 75 km and is an order of magnitude greater than the martian atmosphere at 95 km. This would explain the similar ablation effect of meteors on Mars and Earth. The slightly thinner atmosphere at this level on Mars implies that meteors of larger kinetic energies than on Earth are required for significant ablation to occur above 75 km. The latter would then explain the sporadic occurrence of the meteor layer at its observed altitude.

The gravity field of a planet is the result of its internal mass distribution and rotational state. Rapidly rotating planets bulge at the equator as a result of centrifugal forces. Consequently, the associated redistribution of mass to the equatorial plane results in a stronger gravitational acceleration of a spacecraft when it is near the pole than when it is at the same altitude over the equator. Similarly, anomalies in the internal distribution of mass are expressed as departures of the external gravitational field from that of a uniform sphere or a stratified spherical distribution. Space probes in the vicinity of planetary bodies follow trajectories that deviate from the ideal orbits described by Kepler's laws in response to these gravity anomalies.

The goal of the gravity observations is the study of the state and evolution of the martian crust and lithosphere with important implications for the tectonic evolution and mantle convection of Mars. The targets of investigations are the hot-spot areas Tharsis and Elysium, large single volcanoes such as Alba Patera and Olympus Mons, the large impact craters and basins such as Huygens, Argyre and Hellas, respectively, rift structures like Tempe Fossae and Claritas Fossae, and the highland-lowland boundary. The investigation of impact basins must be viewed in the context of similar studies on other planetary bodies, including Earth, in the sense of comparative planetology and studies of the impact mechanisms that are not yet fully understood, especially for large basins. Studies of the highland-lowland boundary will contribute to the open question of this dichotomy.

Up to June 2005 there were 21 successful target gravity observations in total (Table 5 and Fig. 15). This low number results from the fact that the imaging instruments had priority for high-gain antenna Earth pointing and instrument nadir pointing when requesting the same pericentre target observation as radio science.

The gravity measurements consist of Doppler data along line-of-sight (LOS) near the pericentre above the selected target areas of geophysical interest (Pätzold et al., 2004), as summarised in Table 5. The altitude of Mars Express at pericentre, between 265 km and 330 km, is lower than the minimum altitude (370 km) of the circularised orbit of MGS (Lemoine et al., 2001; Yuan et al., 2001). Short-wavelength orbital perturbations due to gravity are thus significantly larger on MEX than on MGS, so that MEX gravity data are useful for improving knowledge of the short-wavelength gravity anomalies over the observed targets.

Starting from the observed Doppler shift frequencies, LOS Doppler velocity residuals were computed using the latest reconstructed orbit solution provided by ESA's European Space Operations Centre (ESOC); see Fig. 16 for orbit 1144 over Olympus Mons as an example. Since the reconstructed orbit solution computed by ESOC is based on the global gravity field JGM85F02 up to degree and order 50, the resulting Doppler residuals do not include variations caused by gravity harmonics lower than degree and order 51.

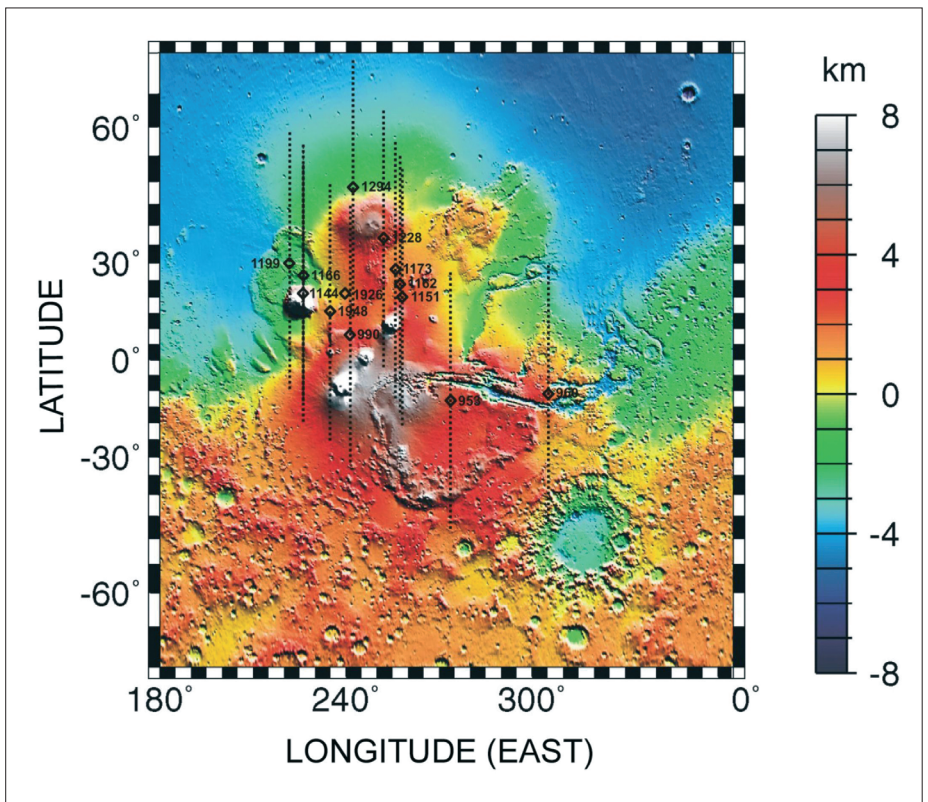
The noise of the Doppler velocity residuals may be estimated from the high-altitude part of the pericentre pass where short-wavelength gravity anomalies have a negligible effect on the spacecraft orbit. For an integration time of 10 s, we obtain a mean value of 0.02 mm/s, which agrees well with the mean noise (0.03 mm/s) on the LOS velocity residuals during the Gravity Calibration Orbit of MGS. The signal-to-noise ratio is thus better than for the MGS LOS data. The pericentre pass is defined by an

## 5. Observations of the Martian Gravity Field

Target	Orbits in 2004 (Oct–Dec)	Orbits in 2005 (first 6 months)
Alba Patera	–	1228, 1239, 1294, 1338
Olympus Mons	1067, 1144, 1166, 1199	–
Tempe Fossae <sup>(a)</sup>	–	1290
Elysium Mons	1013, 1035, 1163, 1174	–
Tharsis volcanoes	990, 1074, 1151, 1162, 1173	–
Valles Marineris	953, 960, 993	–
Hellas	–	–
North Polar Cap <sup>(b)</sup>	–	–

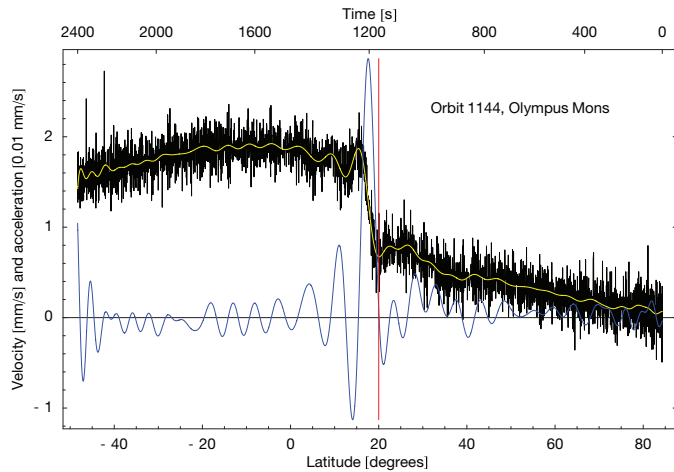
<sup>(a)</sup>not obtained in 2004 owing to a pointing conflict with the Omega instrument  
<sup>(b)</sup>most of the pericentres over the North Polar Cap could not be observed because the eclipse covered the pericentre pass; the observations of the remaining two orbits start after the pericentre

Fig. 15. The Olympus Mons/Tharsis Ridge area with the locations of the pericentres and tracks recorded for gravity studies.



observation time of  $\pm 20$  min around the pericentre (i.e. an altitude of 1375 km), but the perturbation due to gravity anomalies beyond harmonic degree 50 is negligible with respect to the noise level above an altitude of 500 km. Thus only the low-altitude part ( $< 500$  km) is kept for the comparison with the predictions from the gravity field; the upper part is used for the noise reference.

LOS velocity residuals are differentiated into accelerations which can be compared to accelerations predicted by the spherical harmonic global field JGM85F02, and by the uncompensated topography at each spacecraft position and projected along the



**Fig. 16.** Velocity residuals translated from the Doppler frequency residuals at X-band. The Doppler frequency residuals were computed from the received frequency at X-band minus the predicted frequency for the reconstructed orbit. Shown here are the velocity residuals from pericentre pass 1144 over Olympus Mons.

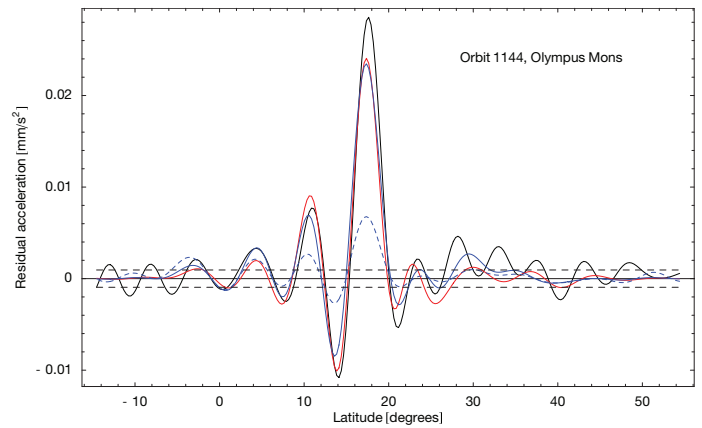


**Fig. 17.** Filtered acceleration residuals computed from the velocity residuals from orbit number 1144 (thick black continuous curve), acceleration due to the uncompensated topography (red dotted curve), prediction of the global gravity field JGM85F02 at the altitude of MEX (blue continuous curve) and at the altitude of MGS (dashed blue curve). The noise level on the filtrated acceleration residuals of this profile is indicated by the dash-dotted curve.

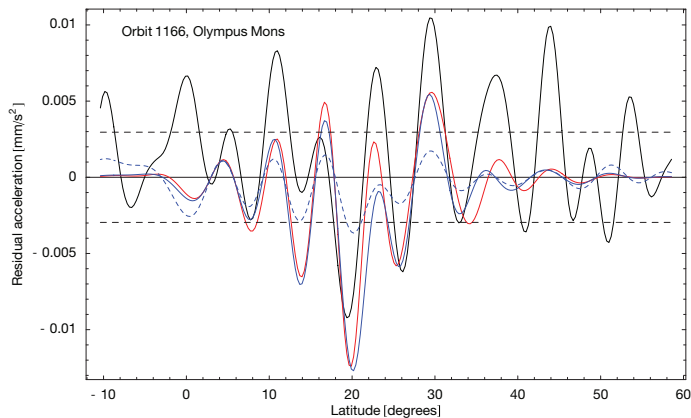


**Fig. 18.** As Fig. 17, but for orbit 1166.

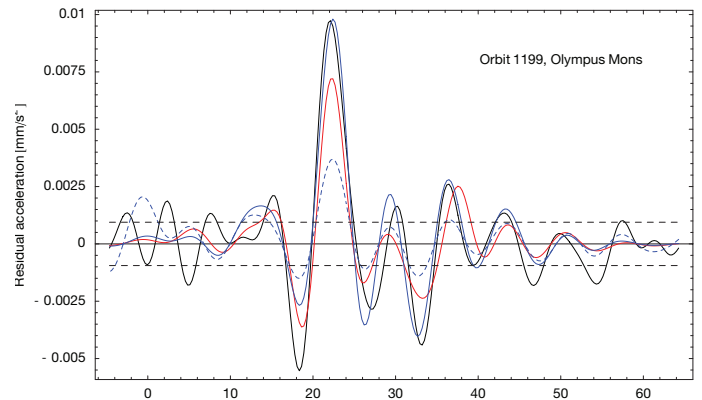


**Fig. 19.** As Fig. 17, but for orbit 1199.

line-of-sight direction. Figures 17–19 are examples of the acceleration above Olympus Mons (computed from tracks similar to those shown in Fig. 16). The acceleration observed by Mars Express (thick continuous black curve) can be compared with the acceleration predicted by the global gravity field JGM85F02 (blue continuous curve) as well as with the acceleration that would be felt if the spacecraft were at the minimum MGS altitude of 370 km with the same groundtrack. The residual gravitational acceleration can be seen to be several times larger for Mars Express than for an MGS-like orbit. The observed acceleration has a good correlation with the acceleration from the uncompensated topography (red dotted curve), except at high frequency because the observational noise is present at all frequencies, whereas the acceleration computed from the topography can be considered as noiseless. The power of the observed acceleration is larger than the power of the acceleration from the uncompensated topography, which might suggest a higher crustal density at Olympus

Mons. The confidence in such geophysical predictions is, however, limited by the presence of noise, and only the accumulation of several parallel orbits above a target improves the quality of the prediction by statistically decreasing the noise. In the three examples shown in Figs. 17-19, orbits 1144 and 1199 support the high crustal density hypothesis, whereas orbit 1166 has a too-high noise level to be useful.

In their analysis of MEX gravity data, Beuthe et al. (2005) performed a comparative spectral analysis of the MEX and MGS accelerations and the theoretical acceleration from a model of the topography. They computed the coherences between the MEX and topography accelerations, between the MGS and topography accelerations, and between the MEX and MGS accelerations. The average coherence MEX/topography is optimal down to a wavelength corresponding to the altitude of the spacecraft at pericentre; it rapidly decreases for much smaller wavelengths because of the presence of noise in the MEX residuals. This behaviour corresponds to expectations based on the rule of thumb that the smallest detectable wavelength is given by the minimum altitude of the spacecraft. The global MGS gravity solution shows a coherence with the topography comparable to MEX or better, because the global gravity field is obtained as a statistical average over thousands of MGS profiles. The MEX/MGS coherence is similar in shape to the MEX/topography coherence, though a little smaller at large wavelengths because of unmodelled effects in the MEX orbit. This coherence remains at a high level down to a wavelength of 300 km.

The gain factor between MEX and MGS is 1 within the error bars, except again at the largest wavelength, where the coherence is lower. This analysis of the coherence and gain factor shows that MEX can be used as an independent check on the quality of the existing gravity solutions such as JGM85F02 in the target regions analysed at an altitude lower than MGS orbits. Conversely, the good agreement between MEX and MGS also provides confidence in MEX gravity data.

Several parallel pericentre tracks over a target area, if available, will be used for a refined analysis of the local structure of the crust and the lithosphere, in order to obtain, for instance, the local crustal density. Just this local crust density has a very strong effect on the acceleration signal at short wavelengths and MEX is very sensitive to that.

In parallel, gravity data from MEX apocentre passes are used to derive temporal variations of the gravity field from seasonal mass exchange. A large amount of data is required in order to be able to observe seasonal effects. From October to December 2004, 36 passes of up to 3 h could be obtained, with another 135 passes in the first half year of 2005. These data are being processed with the GINS software package in Brussels and will be grouped and averaged in monthly or quarterly batches to derive a mean  $C_2O$  and  $C_3O$  over the respective time span. Changes in the averaged coefficients will give indications on seasonal mass exchange between the poles, and variations in rotation.

These apocentre data will also be used in an attempt to determine the  $k_2$  Love number. This number represents the non-rigid Mars response to the tidal potential and can be seen from the orbit of Mars Express. A strategy to separate the various parameters has been developed and will be applied to all data.

## 6. Bistatic Radar Observations

Two bistatic radar experiments were conducted during the first year of Mars Express operations. Four more were conducted during the first half of 2005, and others were made at the rate of approximately two per month through the remainder of 2005. The first was carried out on 21 January 2004 when the spacecraft was near apoapsis on orbit 36; it yielded no S-band surfaces echoes (12.6 cm wavelength) but had strong echoes at X-band (3.6 cm). Unfortunately, the ground calibrations failed, and it has been impossible to obtain results that are quantitatively meaningful. After overhauling the calibration procedures, the second experiment was conducted on 21 May 2004 (orbit 422). This yielded very weak S-band echoes despite an Earth-Mars distance of more than 2 AU, but there was nothing at X-band because of a receiver tuning error. No further experiments were attempted during the remainder of 2004 as Mars passed

Table 6. Bistatic radar observations in 2005.

Date	Orbit	Ground Station	Target location	Specular Point			Dielectric Constant $\epsilon$	
				Longitude E. (deg)	Latitude N. (deg)	Incidence angle (deg)	S-band ( $\lambda=13$ cm)	X-band ( $\lambda=3.6$ cm)
22 May 04	426	DSS 14	Vastitas Borealis	60.1	64.1	59.9	2.7	N/A
27 Feb 05	1430	DSS43	Argyre SE rim	321.4	-57.3	61.7	2.14	2.02
3 Apr 05	1555	DSS43	Southern Highlands	289.9	-50.8	51.11	3.52	3.19
10 Apr 05	1583	DSS43	Hellas	63.7	-42.7	51.9	TBD	TBD
24 Apr 05	1631	DSS14	South of Hellas	261.7	13.9	68.0	TBD	TBD
06 Jul 05	1893	DSS43	South of Hellas	74.9	-60.9	64.9	2.75	2.58
24 Jul 05	1956	DSS14	Northern Plains	155.9	49.4	70.0	TBD	TBD
26 Aug 05	2075	DSS 14	South Pole	-45.16	-87.36	75.31	TBD	TBD
27 Aug 05	2078	DSS 14	South Pole	33.20	-87.39	74.96	TBD	TBD
31 Aug 05	2091	DSS 63	South Pole	-86.72	-89.75	76.95	TBD	TBD
6 Sep 05	2113	DSS 63	South Pole	-52.90	-87.10	76.66	TBD	TBD
1 Oct 05	2202	DSS 14	Utopia Planitia	118.87	49.54	61.15	TBD	TBD
19 Oct 05	2267	DSS 14	Arcadia Planitia	-151.30	47.41	60.58	TBD	TBD

TBD: to be determined

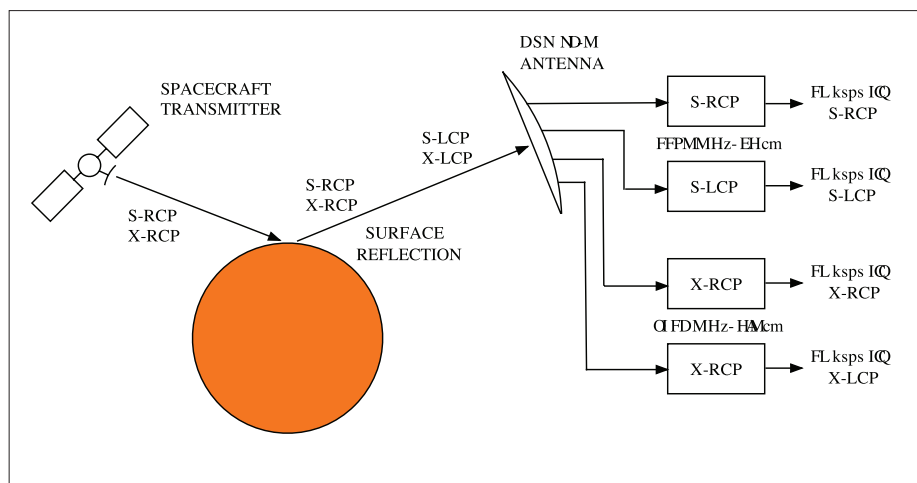


Fig. 20. Signal flow for Mars Express bistatic radar. RCP signals are transmitted; the reflection process converts some of the RCP to LCP.

through superior solar conjunction. Nearly a dozen experiments were conducted in 2005; all were successful (Table 6).

For the experiment on 21 January 2004, the spacecraft's high-gain antenna (HGA) was pointed toward the martian surface from a distance of 12 800 km, radiating 5 W and 60 W at the S- and X-band, respectively, while NASA's 70 m DSN antenna near Canberra, Australia, captured the echoes. The microwave signals were translated into audio frequencies, sampled at 25 000/s (complex), and stored for later digital processing (Fig. 20).

During surface reflection, right-circularly polarised (RCP) signals from the transmitter are converted into a combination of RCP and left-circularly polarised (LCP) echoes. The relationship between RCP and LCP may be used to infer properties of the surface material at each frequency, such as through the Fresnel reflection

Fig. 21. The specular point track is the locus of boresight intercepts with the surface had the HGA pointing been optimised for maximum echo strength as a function of time. For this experiment, HGA pointing was fixed in inertial space for the duration of the experiment. The boresight swept across the surface approximately as shown by the red line, intersecting the specular track at 05:50 Earth-receive time (ERT). The half-power HGA footprint on the surface at 05:50 was an ellipse of semi-major axis 400 km oriented 60°W of N and towards Mars Express; Earth was towards the ESE. The semi-minor axis was 150 km.

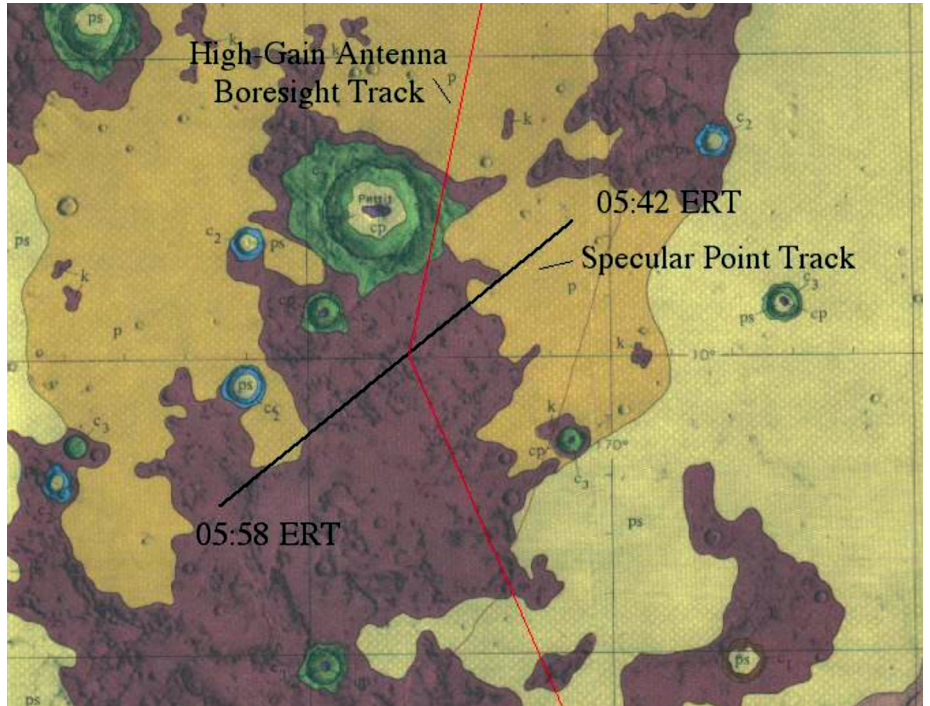


Table 7. Geometrical and performance parameters for the bistatic radar.

	X-RCP	X-LCP	S-RCP	S-LCP
Carrier Frequency $f_c$ (MHz)	8420	8420	2296	2296
Carrier Wavelength $\lambda$ (m)	0.036	0.036	0.131	0.131
Incidence/Reflection Angle (deg)	68.1	68.1	68.1	68.1
Transmitted Power $P_t$ (w)	60	0	5	0
Transmit Antenna Gain $G_T$ (dBi)	40	–	28	–
Spacecraft to Specular Point Distance $R_t$ (km)	12800	12800	12800	12800
Specular Point to Earth Distance $R_R$ (km)	$1.94 \times 10^8$	$1.94 \times 10^8$	$1.94 \times 10^8$	$1.94 \times 10^8$
Receiving Antenna Gain $G_R$ (dBi)	74.1	74.1	63.3	63.3
Effective Receiving Aperture $A_R = \lambda^2 * G_R / 4\pi$ (m <sup>2</sup> )	2600	2600	2900	2900
Receiver System Temp $T_{sys}$ (K)	30	30	20	20
Receiver Noise Power $N_0 = kT_{sys}$ (W/Hz)	$4.14 \times 10^{-22}$	$4.14 \times 10^{-22}$	$4.14 \times 10^{-22}$	$4.14 \times 10^{-22}$

coefficients (Simpson, 1993; Simpson & Tyler, 2001). For example, a dielectric constant of 3.0 would show equal power in orthogonal echo polarisations if reflection occurred at the Brewster angle  $\phi_B = 60^\circ$ .

To simplify spacecraft operations, the HGA was pointed in a fixed direction such that the specular point on Mars would be along the HGA boresight at transmit time  $t_0 = 05:39:14$  (incidence angle  $\phi_i = 68.1^\circ$ ). At receive time  $t_0 = 05:50:00$  the corresponding reflected signal reached Earth. More than 30 min of data were recorded both before and after, showing the rise to and decay from the specular condition. At  $t_0$  the 3 dB HGA footprint on Mars was an  $800 \times 300$  km ellipse centred on  $10.0^\circ N, -173.5^\circ E$  (Fig. 21).

The 25 kHz bandwidth from each receiver may be processed to arbitrary frequency resolution; the spectral shape may be ‘equalised’ to correct for characteristics of filters in the receiving system, and the background radiothermal noise may be calibrated. The last step is critical to correct inference of the surface dielectric constant.

For each frequency and polarisation, the echo power  $P_R$  reaching Earth may be derived from the bistatic radar equation

$$P_R = (P_T G_T / 4\pi R_T^2) \sigma (A_R / 4\pi R_R^2) \quad (12)$$

where  $P_T$  is the power transmitted by the spacecraft,  $G_T$  is the gain and radiation pattern of the HGA,  $R_T$  is the distance of the spacecraft from Mars’ centre of mass,  $A_R$  is the effective aperture of the receiving antenna,  $R_R$  is Earth–Mars distance, and  $\sigma$  is the target radar cross section, which is proportional to the Fresnel reflectivity:

$$\begin{aligned} \rho_R &= 0.25 (R_V + R_H)^2 && \text{RCP received, or} \\ \rho_L &= 0.25 (R_V - R_H)^2 && \text{LCP received} \end{aligned}$$

The ‘horizontal’ and ‘vertical’ reflection coefficients are, respectively,

$$\begin{aligned} R_H &= (\cos\phi_i - (\epsilon - \sin^2\phi_i)^{1/2}) / (\cos\phi_i + (\epsilon - \sin^2\phi_i)^{1/2}) \\ R_V &= (\epsilon \cos\phi_i - (\epsilon - \sin^2\phi_i)^{1/2}) / (\epsilon \cos\phi_i + (\epsilon - \sin^2\phi_i)^{1/2}) \end{aligned}$$

where  $\epsilon$  is the dielectric constant of the surface material.

If the echo power can be measured accurately, Eq. (12) may be worked backwards to obtain  $\epsilon$  using values such as those in Table 7. The functional form of  $\sigma$  and the radiation pattern of the HGA ( $G_T$ ) are not well known, but they are common to the evaluation of  $P_R$  for either polarisation. Similar comments apply to  $P_T$  and  $A_R$ . Calculation of the ratio of  $P_R$  for RCP to  $P_R$  for LCP simplifies the process at the expense of needing well-calibrated measurements in both polarisations.

In the typical output from a bistatic radar receiver (Fig. 22), there are spectral ranges with only noise power that is produced by the cosmic background, the atmosphere (especially clouds and precipitation), the antenna structure and the receiving electronics. Although not used routinely in spacecraft telecommunications, instrumentation and procedures exist for determining the level of this noise and for apportioning it to each source.

For purposes of the bistatic radar 25 kHz bandwidths, the background noise is constant across the spectrum and can be characterised by a system temperature  $T_{\text{sys}}$  such that the noise power at any frequency is  $P_N = kT_{\text{sys}}B$ , where  $B$  is the measurement resolution in frequency. From a data spectrum,  $P_N$  is the height of the noise pedestal upon which the surface echo and residual carrier ride; the absolute powers in the echo and carrier can be determined relative to  $P_N$ .

In Fig. 22 the bandpass filter characteristics have been compensated for, the noise pedestal has been removed, and the echo and carrier powers have been normalised by  $P_N$ . Unfortunately, the calibration procedure for determining  $P_N$  was not executed correctly on any of the receiver channels, so values of  $P_R$  are uncertain by factors of at least 2. To illustrate the technique and its application in more recent experiments, the remaining steps in the procedure are continued with, but the quantitative results for 21 January must be considered as highly suspect.

Figure 23 shows the integrated X-band surface echo power as a function of time for RCP and LCP. A default  $T_{\text{sys}} = 30\text{K}$  was assumed for both polarisations, but experiments in 2005 returned values closer to 20K for both. There is also evidence that a calibration source, which could have added as much as 30K to the apparent background noise in one channel, may have been accidentally left on during the January 2004 observations. With the default  $T_{\text{sys}} = 30\text{K}$  we find almost identical RCP and LCP powers, which translates to  $\epsilon = 5.8$  at the specular angle  $\phi = 68.1^\circ$ . If the measured RCP to LCP power ratio is too small by a factor of 2.5, the inferred

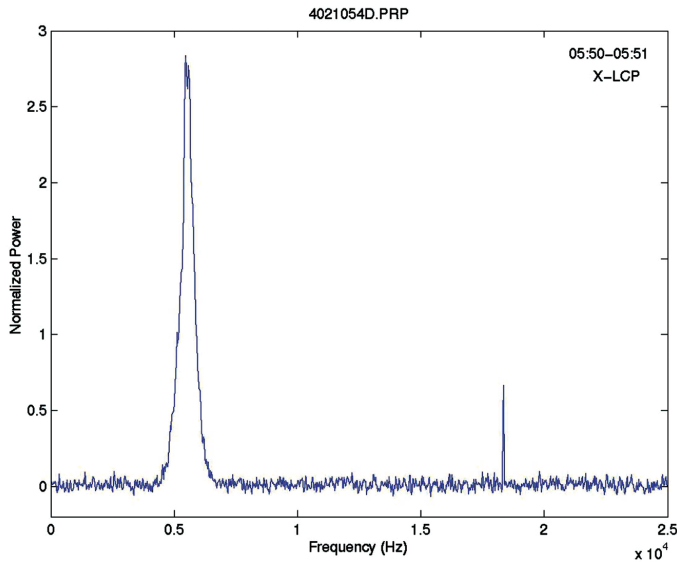


Fig. 22. A 60 s average spectrum from the X-band LCP receiver on 21 January 2004. The broad signal centred on 5500 Hz has been specularly reflected from near (10.0°N, -173.5°E); the narrow signal near 18 000 Hz is a directly propagating carrier residual radiated via an HGA sidelobe. The two signals are separated in frequency because the Doppler effect along the direct and carom paths is different.

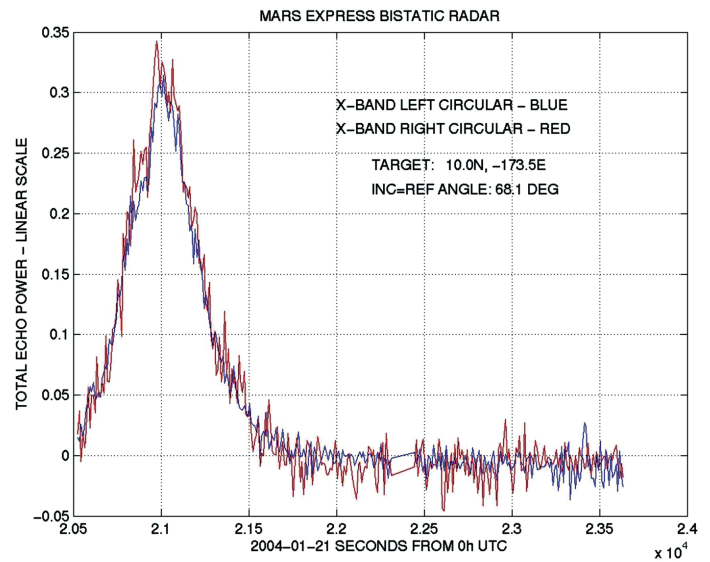


Fig. 23. Total echo power in RCP (red) and LCP (blue) estimated using a default  $T_{\text{sys}} = 30\text{K}$ . At 05:50 (21 000 s) ERT, the HGA boresight intersected the specular point track and echo power reached its maximum. The relative power in the two channels is likely in error by a factor of two or more because of a failure in the calibration system during the observations.

dielectric constant is  $\epsilon \sim 3$ , which is much closer to values reported elsewhere (Pettengill, 1978; Simpson, 1993).

Extensive revisions to the calibration procedures were carried out between January and May 2004. The procedure implemented for the bistatic radar experiment on 21 May appeared to be accurate at a level of about 5% in  $T_{\text{sys}}$ . Given the failure to detect S-band echoes in January, the weak S-band signals found in the May data were surprising. By averaging all of the signal in each polarisation, a dielectric constant of  $\epsilon \sim 2.7$  is inferred from these data, but the error bars are almost as large as the value itself. The target was at 64.1°N, 60.1°E and was observed at an incidence/reflection angle  $\phi = 59.9^\circ$ . An X-band echo may have been present, but an error in tuning the ground receiver left it outside the window that was sampled and recorded in both polarisations. These and more recent results are summarised in Table 6 and Simpson et al. (2005).

## 7. Phobos Observations

The scientific objective of observing Phobos is to determine precisely its mass and its low-order gravity field harmonics. The current values of the Phobos mass vary by 40% (Table 8). The first mass determinations were obtained by Tolson et al. (1977) and Christensen et al. (1977) using the flybys of Viking-1. Since then, many efforts have been made to improve these mass determinations. Combinations of flybys have been used, involving the Viking-1 and Phobos-2 spacecraft. Although the studies did converge on an unexpectedly low value, no real agreement between the various values could be found. A better determination of the mass (and thus the density) would be of great importance towards solving the puzzling origin of the martian satellites. Moreover, current estimates of Mars' internal dissipation, deduced from Phobos' orbital acceleration, are directly dependent on the accuracy of Phobos' mass.

Obviously, as can be deduced from Table 8, knowledge of the mass is not very precise. Although Kolyuka et al. (1990) constrained their mass determination within an error bar of only 0.69% (using exclusively the Phobos-2 data), none of the three

Author	GM Phobos ( $10^{-3} \text{ km}^3 \text{ s}^{-2}$ )	Volume ( $\text{km}^3$ )	Density ( $\text{g/cm}^3$ )
Tolson et al., 1977	$0.73 \pm 0.07$	–	–
Christensen et al., 1977	$0.66 \pm 0.08$	–	–
Williams et al., 1988	$0.85 \pm 0.07$	5751	$2.2 \pm 0.2$
Kolyuka et al., 1990	$0.722 \pm 0.005$	–	–
Duxbury et al., 1991	–	$5680 \pm 250$	$1.90 \pm 0.05$
Thomas, 1993	–	$5748 \pm 190$	
Smith et al., 1995	$0.587 \pm 0.033$		
Yuan et al., 2001	$0.714 \pm 0.019$		

values published in Kolyuka et al. (1990), Williams et al. (1988) and Smith et al. (1995) fits within a range of 40%. Some bias has to be considered in the processing, especially as different values of Mars' mass may have been used. The observation by Kolyuka et al. (1990) has to be considered as unverified and the measurement error as highly unrealistic.

The martian gravity field is now better constrained than it was during the Viking and Phobos-2 missions. This error can be avoided in future data processing and analysis, so that the Mars Express flybys can be used to their full potential.

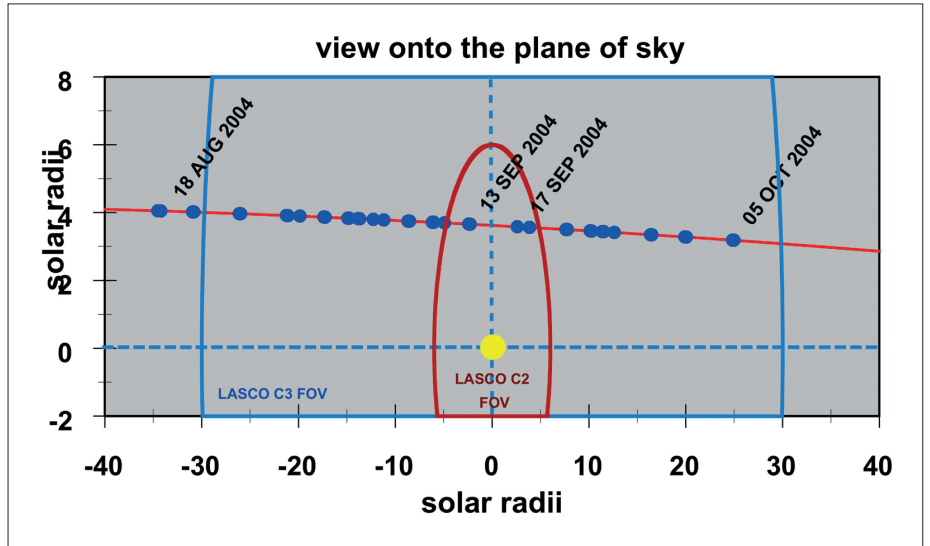
The shift between the centre of mass and the centre of figure ( $J_1$  coefficient in the expansion of the gravity potential) can be determined by a very close flyby. Mass displacements inside the moon (especially following the Stickney impact) would be an indication of internal stress. Such data would bring into question the key point of an assumed (but still not demonstrated) homogeneous density. The higher harmonics, like the  $J_2$  and  $C_{22}$  coefficients, may also be analysed because their dynamical effects have already been observed (but not studied) in Viking residuals (Williams et al., 1988). This will resolve the question of homogenous density versus an internal density distribution. Images from the High Resolution Stereo Camera (HRSC) of Mars Express will provide a precise value for the volume of the body, leading to a precise determination of the bulk density with an accuracy of the order of the volume accuracy.

The latest Phobos observations by HRSC show a 12 km shift between the observed and expected positions of the moon. The Royal Observatory in Brussels, Belgium, is working on new ephemerides from HRSC observations combined with other astrometric observations in order to correct this discrepancy.

Future RS observations during Phobos flybys, in combination with other instrument observations, will improve knowledge of the moon's mass and density by at least an order of magnitude. This will give important clues for the explanation of the origin of Phobos and improve the precision of the martian internal dissipation factor. The observations will also provide with high probability the  $J_1$  coefficient and therefore a measure of the difference between the centre of mass and centre of figure.

To achieve this goal, MaRS requires a very close flyby of Phobos. During the prime mission, this occurred only on orbit 756, with a closest approach of 140 km. In that instance, the optical instruments received priority for this extraordinary flyby, and no radio observations were obtained. All the other comparable opportunities in 2004 and into 2005 occurred behind the planetary disc as seen from Earth and so were not visible from a ground station. Two other opportunities in June 2005 were identified to come within 300 km and be visible. Unfortunately, the first had to be cancelled owing to deployment of the MARSIS antenna. The second occurred at a distance of 900 km

Fig. 24. Geometry of the first MEX solar conjunction, from 15 August to 15 October 2004 within 40 solar radii of the solar disc. The red solid line is the track of Mars in the plane of sky; the blue dots mark the tracking of Mars Express. The blue and the dark red lines show the fields of view of the SOHO LASCO C3 and C2 coronagraphs, respectively.



because the spacecraft orbit had drifted after the first MARSIS antenna deployment and was not corrected before the full MARSIS deployment.

### 8. Observations of the Solar Corona

In addition to the investigations of the atmosphere and gravitational field of Mars, the experiment is also characterising the Sun’s corona. This type of radio-sounding investigation was carried out by several spacecraft in the past and has significantly contributed to understanding the Sun (Bird et al., 1994; Pätzold et al., 1995; Pätzold et al., 1996; Pätzold et al., 1997; Karl et al., 1997).

The radio instrumentation aboard Mars Express is ideal for solar corona studies. With dual-frequency downlinks (simultaneous and coherent S- and X-band downlinks) and the clear detectability of RCP and LCP in both frequency bands (designated X-RCP, X-LCP, S-RCP and S-LCP), estimates of the electron density can be made, along with broad characterisations of average values of the magnetic field as a function of distance from the Sun’s disc.

Mars went into superior solar conjunction on 15 September 2004; the Earth-Mars distance was its maximum 2.6 AU. As seen from Earth, Mars appeared to be located about 3.7 solar radii above the north pole of the solar disc in the plane of the sky (Fig. 24).

Solar corona RS data were acquired during a 39-day period from 18 August to 22 October. Fig. 24 shows the positions of the observations in the plane of sky. On all but five of the observation days, recordings were performed by the 70 m DSN antenna near Madrid, Spain. At this station, typically, four recording channels were available and it was possible to record both the RCP and LCP at X- and S-band. On the other five days, recordings were taken at a 34 m antenna at the Goldstone, California DSN complex (DSS-15), where only RCP channels were available.

The MEX radio signals propagated through the hot, dense and turbulent plasma of the solar corona. The propagation causes a phase advance in frequency and a propagation delay of the ranging signals according to:

$$\Delta f = f_0 \frac{v_r}{c} - \frac{40.31}{c} \frac{1}{f_0} \int_{\text{spacecraft}}^{\text{Earth}} \frac{dN_e}{dt} ds$$

$$\tau = \frac{s}{c} + \frac{40.31}{c} \frac{1}{f_0^2} \int_{\text{spacecraft}}^{\text{Earth}} N_e ds$$
(13)

where  $\Delta f$  is the recorded Doppler shift consisting of the classical Doppler shift (first term) and the propagation in plasma (second term),  $\tau$  is the propagation time of the radio signal between the spacecraft and the ground station consisting of the vacuum light time (first term) and the propagation delay in plasma (second term), and  $N_e$  is the electron density in the solar corona,  $dN_e/dt$  is the temporal change of electron density at time scales of the integrated sampling time,  $f_0$  is the radio carrier frequency,  $v_r$  is the relative velocity between the receiver on Earth and the spacecraft transmitter, and  $s$  is the distance (range) between the ground station and the spacecraft.

By using two frequencies, e.g. X-band and S-band, simultaneously and forming the differential Doppler and differential range, the contribution of the plasma to the one-way downlink at the lower frequency is yielded, here at S-band

$$\Delta f_s - \frac{3}{11} \Delta f_x = -\frac{40.31}{c} \left\{ \frac{1}{f_s^2} - \frac{1}{f_x^2} \right\} f_s \int_{\text{spacecraft}}^{\text{Earth}} \frac{dN_e}{dt} ds$$

$$\tau_s - \tau_x = \frac{40.31}{c} \left\{ \frac{1}{f_s^2} - \frac{1}{f_x^2} \right\} \int_{\text{spacecraft}}^{\text{Earth}} N_e ds$$
(14)

From the Ulysses superior solar conjunctions in 1991 and 1995 (Bird et al., 1994; Pätzold et al., 1995) and the experiences gained in these experiments, MaRS defined the solar conjunction phase within a range of 40 solar radii ( $10^\circ$  elongation) about the solar disc in the plane of sky. Mars entered this range on 15 August and exited on 15 October 2004.

MaRS requested one tracking pass per day with the spacecraft transponder and ground station configured as S-band uplink, X-band and S-band simultaneous downlink; dual-frequency ranging where feasible (DSN only). Although the first passes in August were conducted at S-band uplink, ESOC switched back to X-band uplink for operational reasons after a few passes. The total number of passes was 34 (instead of the 60 projected), each of a few hours but sometimes only 20 min. They were performed exclusively by the DSN, with the majority at the 70 m station DSS-63 in Madrid. The recording bandwidth in DSN's open-loop RS Receiver was 2 kHz, allowing capture of signal dynamics not modelled in the frequency predictions and signal broadening resulting from propagation through the solar corona.

Spacecraft signal parameters sensitive to changes in the propagation medium include frequency Doppler shift, ranging, bandwidth, amplitude/phase scintillations and Faraday rotation (Bird, 1982). The MEX 2004 solar corona experiment data will be processed in full to examine all these effects.

Figure 25 shows six SOHO LASCO C3 images centred about solar conjunction. The varying coronal structure with streamers and holes is prominent. The position of Mars is a faint spot indicated by arrows in the first and last two images. Mars entered and left the field of view of the LASCO C2 images (6 solar radii) on 11 September and 19 September, respectively. Figure 26 shows the four LASCO C2 images, which correspond to the four observations within 6 solar radii.

The change in electron content as a function of solar offset also clearly shows the sounding of coronal streamer and coronal hole structures (Fig. 27). From the SOHO images it can be seen that the position of Mars in the field of view coincided with streamer structures at distances between 20 and 10 solar radii during ingress. While passing over the northern pole within 10 solar radii, less plasma was found and the electron content decreased. This can be followed in Figs. 25 and 26. During superior conjunction, polar rays must have been sounded because the electron content increased again, only to drop again when another coronal hole was encountered (Fig. 26, lower row).

It is concluded from the signature in the differential Doppler and the electron content time series on 21 September 2004 that a coronal mass ejection (CME) may

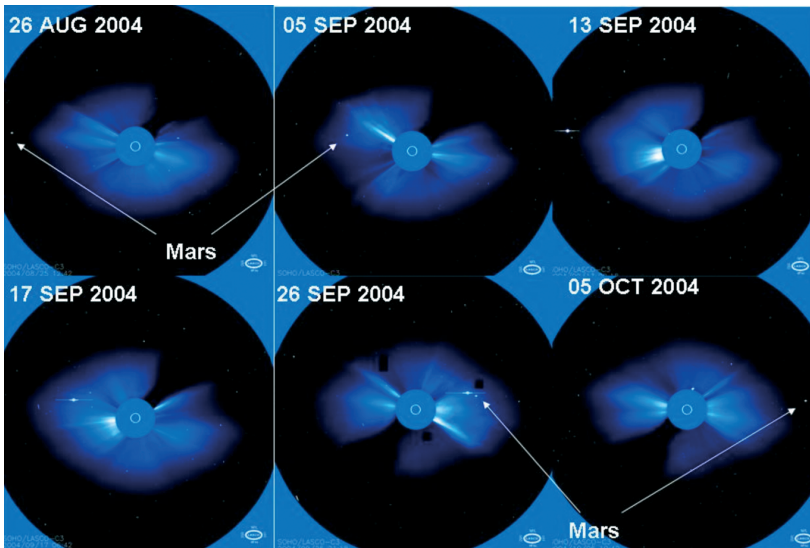


Fig. 25. LASCO C3 coronagraph images (FOV 30 solar radii) showing the coronal structure for the days noted. Mars is marked by arrows. On 13 and 17 September, Mars was behind the inner C3 cover that masks the solar disc. The bright spot in these images is Venus.

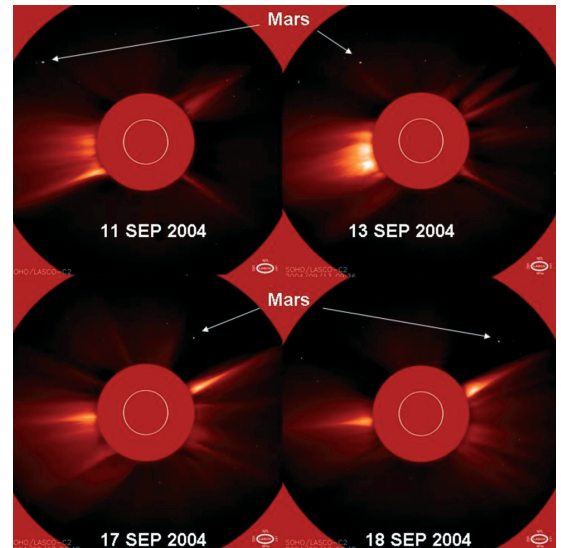


Fig. 26. LASCO C2 coronagraph images (FOV 6 solar radii) from 11–18 September, the four days when Mars Express was tracked within 6 solar radii. The location of Mars is indicated by arrows.

have intersected the radio ray path. Unfortunately, no LASCO images were available for a period of 62 h from 20 September to 23 September to cover that event.

The CME signature is easily extracted from the X-band and S-band residuals and the differential Doppler (Fig. 28). A fast-moving plasma shock front crossing both uplink and downlink can be identified:

- in the downlinks because both frequencies are affected;
- in the differential Doppler representing the downlink at S-band;
- on the uplink at X-band and a time  $\Delta t$  later again on the X-band downlink repeating the signal;
- not on the S-band downlink after  $\Delta t$  seconds because the uplink frequency is downconverted by a factor of 240/749.

The integration of the differential Doppler yields the change in electron content along the ray path since the start of the measurement. A strong increase in electron content by 8000 hexem can be seen for the duration of the signature at X-band starting at 1600 s (Fig. 28); this is in comparison to typical changes in electron content in the solar corona by a few hundred hexems.

With these data it is possible to study the morphologies of CMEs in the microwave bands, to determine the position where a CME hits the ray path, its speed and the density of the shock front. These studies continue.

## 9. Outlook for the Extended Mission

The Mars Express Radio Science Experiment has shown that the spacecraft is an efficient and sensitive tool for gravity studies, atmospheric/ionospheric/coronal sounding and bistatic radar. The experiment has achieved outstanding results and made important discoveries despite operational constraints and pointing conflicts. Atmospheric and ionospheric sounding can be done at locations and local times on Mars that are inaccessible to MGS, thereby complementing the numerous MGS observations. The gravity signal is a factor of four stronger during MEX pericentre

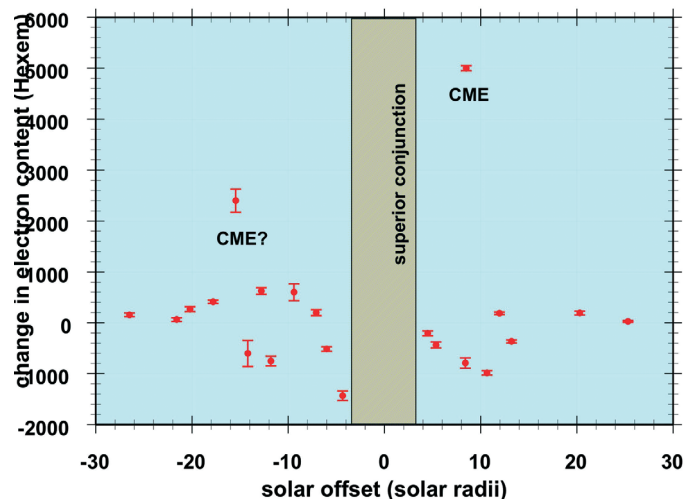
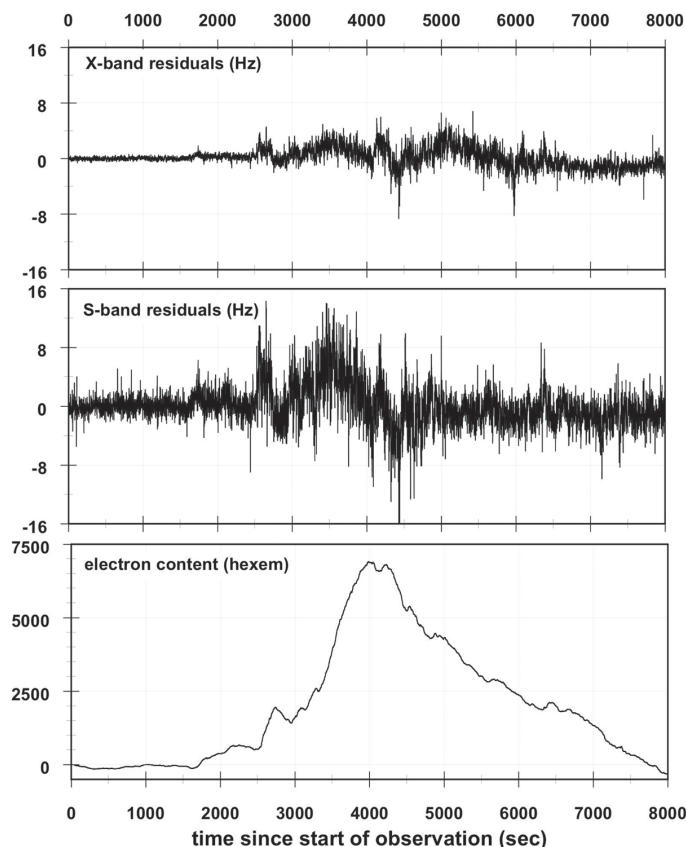


Fig. 27. Change in electron content from dual-frequency Doppler as a function of solar offset. The red circles are the average change in electron content; the error bar marks the maximal variation during the tracking pass. A CME and possibly a second show extreme values.

Fig. 28. X-band and S-band residuals (the two upper panels) from DOY 265, 2004 show the signature of a CME crossing the radio ray path. The lower panel is the change in electron content. A rapid rise in electron content starts with the high density shock front of the CME engulfing the ray path. After the passage of the front, the electron content decreases to normal values.



passes than for MGS. Bistatic radar observations were performed on a regular basis during 2005 and all show strong return echo signals.

The ambitious goals of the MaRS experiment, however, could not be met during the prime mission. This was firstly due to the power situation during eclipses, which resulted in a large number of lost occultations, and, secondly, to the pointing conflicts with the imaging instruments for pericentre gravity observations. The loss of all feasible Phobos observations due to these pointing conflicts was very disappointing.

The mission is in its second extension at the time of this publication, encompassing more occultation seasons and one solar conjunction in 2006. Gravity studies and bistatic radar experiments are being planned as individual events, hopefully at a higher rate than during the prime mission, although constraints and conflicts still remain.

- Angelats i Coll, M., Fotget, F., Lopez-Valverde, M.A. & González-Galindo, F. (2005). The First Mars Thermospheric General Circulation Model: The Martian Atmosphere from the Ground to 240 km. *Geophys. Res. Lett.* **32**(4), CiteID L04201.
- Bauer, S.J. & Hantsch, M.H. (1989). Solar Cycle Variations of the Upper Atmosphere of Mars. *Geophys. Res. Lett.* **16**, 373-376.
- Bird, M.K. (1982). Coronal Investigations with Occulted Spacecraft Signals. *Space Sci. Rev.* **33**, 99-126.
- Bird, M.K., Volland, H., Pätzold, M., Edenhofer, P., Asmar, S.W. & Brenkle, J.P. (1994). The Coronal Electron Density Distribution Determined from Dual-Frequency Ranging Measurements during the 1991 Solar Conjunction of the Ulysses Spacecraft. *Astrophys. J.* **426**, 373-381.
- Beuthe, M., Rosenblatt, P., Dehant, V., Pätzold, M., Haeusler, B., Karatekin, O., Le Maistre, S., Van Hoolst, T. & Barriot, J.-P. (2005) Assessment of the Martian Global Gravity Field at Short Wavelength with Mars Express; Submitted for publication.

## References

- Christensen, E.J., Born, G.H., Hildebrand, C.E. & Williams, B.G. (1977). The Mass of PHOBOS from Viking Flybys. *Geophys. Res. Lett.* **4**, 555-557.
- DSMS Telecommunications Link Design Handbook 202 (2000). 34-m and 70-m Doppler, 810-005, Rev. E, 30 November 2000.
- Fjeldbo, G. (1964). Bistatic Radar Methods for Studying Planetary Ionospheres and Surfaces. SU-SEL-64-025, Stanford Electronics Laboratory, Stanford University, USA.
- Fjeldbo, G. & Eshleman, V.R. (1968). The Atmosphere of Mars Analyzed by Integral Inversion of the Mariner IV Occultation Data. *Planet. Space Sci.* **16**, 1035-1059.
- Häusler, B., Eidel, W., Hagl, D., Remus, S., Selle, J. & Pätzold, M. (2003a). Venus Express Radio Science Experiment VeRa, Reference Systems and Techniques Used for the Simulation and Prediction of Atmospheric and Ionospheric Sounding Measurements at Planet Venus. VEX-VERA-UBW-TN-3040, I2.5, 23.07.2004, also Forschungsbericht LRT-WE-9-FB-4, Universität der Bundeswehr München, Germany.
- Häusler, B., Remus, S., Hagl, D. & Selle, J. (2003b). MaRS Experiment System Test Summary Report for FM Transponder, MEX-MRS-UBW-TR-4000, 07.03.2003b, Universität der Bundeswehr München, Germany.
- Hanson, W.B., Sanatani, S. & Zuccaro, D.R. (1977). The Martian Ionosphere as Observed by the Viking Retarding Potential Analyzers. *J. Geophys. Res.* **82**, 4351-4363.
- Hinson, D.P., Simpson, R.A., Twicken, J.D., Tyler, G.L. & Flasar, F.M. (1999). Initial Results from Radio Occultation Measurements with Mars Global Surveyor. *J. Geophys. Res.* **104**(E11), 29997-27012.
- Karl, J., M. Pätzold & M.K. Bird (1997). Coronal Radio Sounding: Non-Gaussian Turbulence in the Source Regions of the Solar Wind. *Geophys. Res. Lett.* **24**, 2881-2884.
- Kolyuka, Y.F., Efimov, A.E., Kudryavtsev, S.M., Margorin, O.K., Tarasov, V.P. & Tikhonov, V.F. (1990). Refinement of the Gravitational Constant of Phobos from Phobos-2 Tracking Data. *Soviet Astr. Lett.* **16**, 168-170.
- Kopp, E. (1997). On the Abundance of Metal Ions in the Lower Ionosphere. *J. Geophys. Res.* **102**(A5), 9667-9674.
- Lemoine, F.G., Smith, D.E., Rowlands, D.D., Zuber, M.T., Neumann, G.A., Chinn, D.S. & Pavlis, D.E. (2001). An Improved Solution of the Gravity Field of Mars (GMM-2B) from Mars Global Surveyor. *J. Geophys. Res.* **106**(E10), 23359-23376.
- Lipa, B. & Tyler, G.L. (1979). Statistical and Computational Uncertainties in Atmospheric Profiles from Radio Occultation – Mariner 10 at Venus. *Icarus* **39**, 192.
- Molina-Cuberos, G.J., Witasse, O., Lebreton, J.-P., Rodrigo, R. & Lopez-Moreno, J.J. (2003). Meteoric Ions in the Atmosphere of Mars. *Planet. Space Sci.* **51**, 239-249.
- Pätzold, M., Karl, J. & Bird, M.K. (1996). Coronal Sounding with Ulysses: Phase Scintillation Spectra in Coronal Holes and Streamers. *Astron. Astrophys.* **316**, 449-456.
- Pätzold, M., Tsurutani, B.T. & Bird, M.K. (1997). An Estimate of Large-Scale Solar Wind Density and Velocity Profiles in a Coronal Hole and the Coronal Streamer Belt. *J. Geophys. Res.* **102**, 24151-24160.
- Pätzold, M., Neubauer, F.M., Carone, L., Hagermann, A., Stanzel, C., Häusler, B., Remus, S., Selle, J., Hagl, D., Hinson, D.P., Simpson, R.A., Tyler, G.L., Asmar, S.W., Axford, W.I., Hagfors, T., Barriot, J.-P., Cerisier, J.-C., Imamura, T., Oyama, K.-I., Janle, P., Kirchengast, G. & Dehant, V. (2004). MaRS: Mars Express Orbiter Radio Science. In *Mars Express: The Scientific Payload* (Ed. A. Wilson), ESA SP-1240, ESA Publications Division, ESTEC, Noordwijk, The Netherlands.
- Pätzold, M., Tellmann, S., Häusler, B., Hinson, D., Schaa, R. & Tyler, G.L. (2005). A Sporadic and Local Third Layer in the Ionosphere of Mars. *Science*; in Press.
- Pettengill, G.H. (1978). Physical Properties of the Planets and Satellites from Radar Observations. *Ann. Revs. Astron. & Astrophys.* **16**, 265-292.
- Remus, S., Häusler, B., Pätzold, M. & Wennmacher, A. (2001). Ergebnisse der Radio Science Testmessungen an den ESA Satelliten Rosetta und Mars Express. Deutscher Luft- und Raumfahrtkongress, DGLR-2001-022, 17-20 September, 2001.
- Rishbeth, H. & Mendillo, M. (2003). Ionospheric Layers of Mars and Earth. *Planet. Space Sci.* **52**, 849-832.

- SGICD (2003). Mars Express Spacecraft/Ground Interface Document, ME-ESC-IF-5001, I 4.4, May 2003, ESA/ESOC.
- Simpson, R.A. (1993). Spacecraft Studies of Planetary Surfaces using Bistatic Radar. *IEEE Trans. Geosci. & Remote Sensing* **31**, 465-482.
- Simpson, R.A. & Tyler, G.L. (2001). Mars Global Surveyor Bistatic Radar Probing of the MPL/DS2 Target Area. *Icarus* **152**, 70-74.
- Simpson, R.A., Tyler, G.L., Pätzold, M. & Häusler, B. (2005). Determination of Local Surface Properties using Mars Express Bistatic Radar. *J. Geophys. Res.*; submitted 2005.
- Smith, D.E., Lemoine, F.G. & Zuber, M.T. (1995). Simultaneous Estimation of the Masses of Mars, Phobos, and Deimos using Spacecraft Distant Encounters. *Geophys. Res. Lett.* **22**, 2171-2174.
- Tolson, R.H., Blackshear, W.T., Mason, M.L. & Kelly, G.M. (1977). The Mass of Phobos. *Geophys. Res. Lett.* **4**, 551-554.
- Wang, J.-S. & Nielsen, E. (2003). Wavelike Structures in the Martian Topside Ionosphere observed by Mars Global Surveyor. *J. Geophys. Res.* **108**(E7), 14-1, CiteID 5078, DOI 10.1029/2003JE002078.
- Williams, B.G., Duxbury, T.C. & Hildebrand, C.E. (1988). Improved Determination of PHOBOS and Deimos Masses from Viking Fly-Bys. *LPI Abstracts* **19**, 1274-1274.
- Woo, R. & Armstrong, J.W. (1979). Spacecraft Radio Scattering Observations of the Power Spectrum of Electron Density Fluctuations in the Solar Wind. *J. Geophys. Res.* **84**(A12), 7288-7296.
- Yuan, D.-N., Sjogren, W.L., Konopliv, A.S. & Kucinskas, A.B. (2001). Gravity field of Mars: A 75th Degree and Order Model. *J. Geophys. Res.* **106**(E10), 23377-23401.
- Yuen, J.H. (1983). *Deep Space Telecommunications System Engineering*. Plenum Press, New York and London.
- Zhang, M.H.G., Luhmann, J.G. & Kliore, A.J. (1990). An Observational Study of the Night Side Ionosphere of Mars and Venus with Radio Occultation Methods. *J. Geophys. Res.* **95**, 17095-17102.

